CrossMark

Multivariate robust modeling and optimization of cutting forces of the helical milling process of the aluminum alloy Al 7075

Robson Bruno Dutra Pereira [1,2] · Rodrigo Reis Leite [3] · Aline Cunha Alvim [3] ·
Anderson Paulo de Paiva [3] · Pedro Paulo Balestrassi [3] · João Roberto Ferreira [3] ·
J. Paulo Davim [2]

Abstract
Helical milling is an advanced hole-making process and different approaches considering controllable variables have been presented addressing modeling and optimization of machining forces in helical milling. None of them considers the importance of the noise variables and the fact that machining forces components are usually correlated. Exploring this issue, this paper presents a multivariate robust modeling and optimization of cutting forces of the helical milling of the aluminum alloy Al 7075. For the study, the tool overhang length was defined as noise variable since in cavities machining, there are specific workpiece geometries that constrain this variable; the controllable variables were axial feed per tooth, tangential feed per tooth, and cutting speed. The cutting forces in the workpiece coordinate system were measured and the components in the tool coordinate system, i.e., the axial and radial forces, were evaluated. Since these two outcomes are correlated, the weighted principal component analysis was performed together with the robust parameter design to allow the multivariate robust modeling of the mean and variance equations. The normal boundary intersection method was used to obtain a set of Pareto robust optimal solutions related to the mean and variance equations of the weighted principal component. The optimization of the weighted principal component through the normal boundary intersection method was performed and the results evaluated in the axial and radial cutting force components. Confirmation runs were carried out and it was possible to conclude that the models presented good fit with experimental data and that the Pareto optimal point chosen for performing the confirmation runs is robust to the tool overhang length variation. Finally, the cutting force models were also presented for mean and variance in the workpiece coordinate system in the time domain, presenting low error regarding the experimental test, endorsing the results.

Keywords Helical milling · Cutting forces · Robust parameter design · Multivariate mean square error · Weighted principal component · Normal boundary intersection

1 Introduction

Machining of holes is a complex task when manufacturing a part. The conventional drilling process presents challenges such as the work material breakouts at hole exit, chip removal, heat dissipation difficulties, and the increasing of thrust forces, which happen due to the extrusion process of material near the tool center point where the cutting velocity is close to zero. Burr on both entry and exit side of the hole, poor dimensional, geometrical, and microgeometrical accuracy are likewise significant due to friction between tool, workpiece, and chip [1–3].

Helical milling has a field of application in aerospace materials, such as aluminum, titanium alloys, and carbon fiber-reinforced polymers (CFRP) materials, and is nowadays widely applied in industry for machining holes with high precision [4–7]. This process presents several benefits regarding the conventional drilling. Because of the helical milling kinematics, cylindrical holes of different diameters can be machined with the same tool. According to Iyer et al. [1], material removal at and near the hole center occurs by cutting rather than

✉ Rodrigo Reis Leite
rodrigo_rl12@hotmail.com

1 Department of Mechanical Engineering–Industrial Engineering, Federal University of São João del Rei, 170 Frei Orlando Square, São João del Rei, MG 36880000, Brazil

2 Department of Mechanical Engineering, University of Aveiro, Campus Santiago, 3810-193 Aveiro, Portugal

3 Institute of Industrial Engineering and Management, Federal University of Itajubá, 1303 BPS Avenue, Itajubá, MG 37500-903, Brazil

by extrusion, resulting in lower thrust force. Low burr formation, little delamination in CFRP, good chip transportation, good cutting fluid conditions, and high-dimensional, geometrical, and microgeometrical accuracy compared with conventional drilling can be achieved [1, 8] facilitating the assembly of mechanical structures. The intermittent cutting process in helical milling is useful for cooling, reducing the risk of tool wear, breakage, or failure arising from elevated temperature. Minimum quantity lubrication (MQL) and air blow could be employed to assist chip transport while in many drilling applications, cutting fluid is used merely to flush the chips from the cutting zone [9].

1.1 Cutting forces in helical milling

The helical milling process is based on a rotating mill, which performs a helical trajectory. According to Fang et al. [10] and Tanaka et al. [11], in helical milling, besides the tool rotation around its own axis, with a related cutting velocity (v_c) in meters/minute, the result of the synchronism between the axial feed of z CNC axis and the interpolation of the xy axes generates the helical path. The borehole diameter (D_b) is determined by the tool diameter (D_t) and the helical diameter (D_h), as shown in Fig. 1. This kinematics allows the generation of different borehole diameters with a single mill by varying the helical path diameter. The helical milling kinematics was previously described [12, 13] and may be defined regarding tangential and frontal cut.

As shown in Eq. (1), the helical feed velocity (v_f) in millimeters/minute can be decomposed into the tangential

feed velocity of the helix (v_{fht}) and the axial feed velocity of the helix (v_{fha}), both in millimeters/minute. The axial feed velocity of the helix can be described considering the axial feed per tooth (f_{za}) in millimeters/tooth, the number of teeth (z), and the spindle rotation speed (n) in revolutions per minute, as in Eq. (2). In the circular trajectory, the tangential feed velocity of the helix (v_{fht})—which is according to Pereira et al. [13] the circular velocity of the tool center point related to the helical diameter (D_h) in millimeter—can be mathematically described in terms of the tangential feed velocity of the cutting edge (v_{ft}) in millimeters/minute, related to bore hole diameter (D_b) in millimeter, as in Eq. (3). The tangential velocity (v_{ft}), expressed in Eq. (4), may be described in function of the tangential feed per tooth (f_{zt}) in millimeters/tooth, the number of teeth (z), and the spindle rotation speed (n) in revolutions per minute.

$$v_f = \sqrt{\left(v_{fha}^2 + v_{fht}^2\right)} \tag{1}$$

$$v_{fha} = f_{za} \cdot z \cdot n \tag{2}$$

$$v_{fht} = v_{ft} \cdot \frac{D_h}{D_b} \tag{3}$$

$$v_{ft} = f_{zt} \cdot z \cdot n \tag{4}$$

In helical milling process, the helical pitch, Eq. (5), is the axial cutting depth (a_p^*) in millimeter, which depends mathematically on the axial and tangential feed velocities. Then, it can be described in terms of the angle of the helix (α), expressed in Eq. (6). The axial cutting depth can be also described considering the axial and tangential feed per tooth, f_{za} and f_{zt}. This decomposition is important to address the effects of the feed on these directions on the cutting force components.

$$a_p^* = \tan(\alpha) \cdot \pi \cdot D_h = \frac{f_{za} \cdot \pi \cdot D_b}{f_{zt}} \tag{5}$$

$$\alpha = \arctan\left(\frac{v_{fha}}{v_{fht}}\right) \tag{6}$$

In cutting force prediction, it is relevant to define two coordinate systems to describe the process tool motion: the workpiece coordinate system and the tool coordinate system [8, 12]. In the workpiece coordinate system, the coordinate axis directions x, y, and z are fixed whereas the tool coordinate system varies with tool rotation and orbital revolution. To address cutting forces in helical milling, it is important to take into consideration these two coordinate systems. The workpiece coordinate system is used for monitoring. The
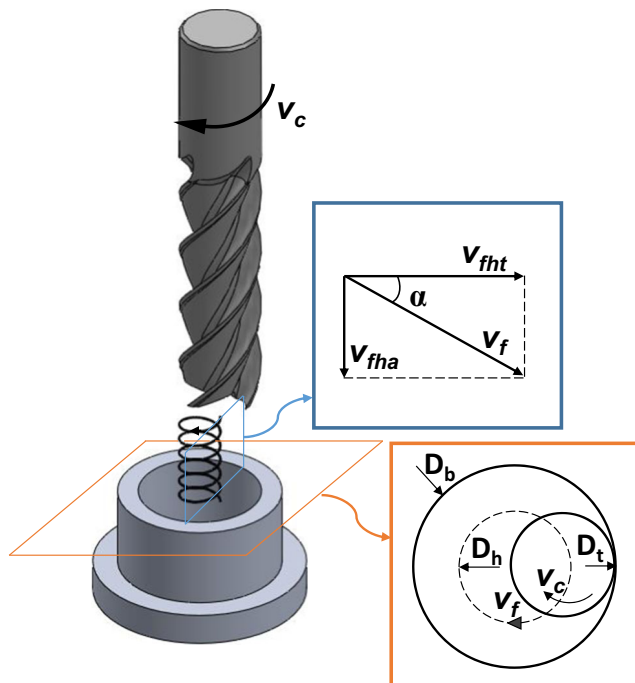

Fig. 1 Helical milling kinematics

components in the tool coordinate system are important to understanding (i) the influence of the cutting parameters in cutting forces and (ii) the correlation among cutting forces and quality parameters, for instance, the dimensional deviation due to radial force.

Predicting cutting forces is important to assure energy economy, workpiece quality, tool integrity, and to reduce machining damage [14, 15]. Cutting forces have a relationship with power consumption and tool wear [16]. In the precision manufacturing of a part, minimizing cutting force levels allows obtaining high-quality parts by minimizing vibrations, tool wear, and tool deflection. Different studies are mentioned in this section to summarize current results about cutting forces trends and modeling in the helical milling process.

Among cutting force components in the helical milling process, the axial force (F_a) acts along the z axis while the radial force (F_r) acts toward the tool center [17]. It is relevant to address F_r because it may lead to tool radial deflection causing vibrations. This is related to geometrical and dimensional deviations and degradation of the surface finish of the hole [18].

Concerning tool cutting edges, the peripheral cutting edge generates mainly F_r, and the front cutting edge generates mainly both F_r and F_a [17]. F_r is also called feed normal force (F_{fN}) [12]. It is a resultant force that can be calculated through the components F_x and F_y, which are cutting forces in the x and y directions on the xy plane of the workpiece coordinate system, $F_r = \sqrt{F_x{}^2 + F_y{}^2}$ [19]. F_a, measured according to the tool coordinate system, is equal to F_z, measured in the workpiece coordinate system [19].

Brinksmeier et al. [8] studied helical milling kinematics and modeled the undeformed chip geometry, considering peripheral and frontal cuts. Denkena et al. [12] assured that in the helical milling process, continuous and discontinuous cuts are presented in peripheral and frontal cut, respectively. This cutting mechanics leads to differences in cutting forces and temperature, generating force levels 10 times lower than force levels in drilling process [9, 20].

Denkena et al. [12] studied cutting force components considering the tool coordinate system (feed force F_f and feed normal force F_{fN}) on CFRP–titanium layer compounds in the helical milling. It was found that the axial feed per tooth increases contributes to the progress of feed force and feed normal force due to an increased pitch of the helical tool path. Consequently, this increases the height of the undeformed chip. The tangential feed per tooth increase leads to decreasing feed and feed normal forces due to a reduction of the height of the undeformed chip.

Shan et al. [20] studied the big pitch influence on machining force components in the helical milling of the aerospace Al-alloy 6061. It was shown that the pitch increase leads to a growth in the axial cutting force component F_z since the axial feed increases with pitch increment.

Liu et al. [21] analytically modeled the cutting forces on side cutting edges and on end cutting edges along the helical feed path considering the tangential and axial feeds of the tool, the spindle rotation, and the interaction between tool and workpiece. However, the experimental results showed percentage error levels from 6.36 to 11.8% of the simulation results.

Ventura and Hassui [14] modeled cutting forces in the helical milling using a circular insert, taking into consideration the tool contact angle and the respective depth of cut. The simulation of F_z and F_y presented similar profiles when compared to the experimental results, despite the observation of some errors, which according to the authors, occurred mainly due to the dynamics of the machine and the used approximations.

Haiyan and Xuda [17] developed a mechanistic cutting force model to improve the cutting force prediction in the helical milling of CFRP. It considered the fiber cutting angle according to helical milling cutting principles. The established model with the cutting force coefficients seemed to be efficient to calculate relative accurate cutting forces in the helical milling of carbon fiber-reinforced polymers.

Wang et al. [19] conducted a comparative study involving stacks of CFRP/Ti versus CFRP and Ti alloy single plate in the helical milling process. Among the obtained results, during the machining of stacks of CFRP/Ti, the cutting force suddenly increased in machining of titanium alloy. That increase is significant if compared to CFRP in the stack and in the single titanium alloy layer. A good justification is the abrasive tool wear during CFRP machining, leading to the increase of cutting force, especially the axial cutting force F_z in titanium stack machining.

Rey et al. [22] developed cutting force models for the helical milling of Ti–6Al–4V titanium alloy with consideration to tool geometry and cutting conditions. They considered the chip geometry regarding cutting conditions and tool geometry and defined a cutting force model based on the instantaneous chip thickness. The models for F_z and F_r achieved errors of 18.8 and 5.35%, respectively.

Li et al. [23] developed analytical cutting force models for side and bottom flutes with cutter runout in helical milling. The results showed the models considering the cutter runout presented errors of 6.09, 10.72, and 13.59% in the x, y, and z directions, which are better results than previous models.

Considering the referred results, it is necessary to obtain better models for cutting force components in the helical milling process. Furthermore, the error levels of the proposed analytical models are usually related to the environmental or noise factors (variables), i.e., the non-controllable factors. Modeling approaches that consider only controllable factors do not take into consideration part of data variability, relative to noise factors, without explanation. This can generate significant error levels in predicting cutting forces. In addition,

cutting force components usually present high correlation structures, which can influence negatively the estimation of regression model coefficients. Therefore, multivariate robust modeling and optimization techniques need to be applied due to the multivariate nature of cutting forces and the presence of noise factors in the helical milling process.

Given the aforementioned discussion, the aim of this paper is to optimize the correlated responses axial and radial cutting force components of the helical milling of the aluminum alloy Al 7075. The independent variables considered were axial and tangential feed per tooth, cutting velocity, and tool overhang length. In this line of reasoning, this work presents a multivariate robust modeling and optimization method ($MMSE_W$-NBI), which is based on the weighted principal component (WPC) technique, robust parameter design (RPD), response surface methodology (RSM), mean square error (MSE), and normal boundary intersection (NBI) optimization methods.

To deal with the correlation structure between the axial and radial cutting forces, the weighted principal component technique was performed yielding principal component scores, which represent the data set of the original correlated responses axial and radial cutting forces. Given these scores, the next step could be carried out, which was the robust parameter design approach and response surface methodology. Performing these techniques, response surface models for the mean and variance equations of the weighted principal component and the axial and radial cutting forces were obtained. As the mean square error optimization technique is an agglomeration strategy of two objective functions into one, leading to the same problems of the weighted sum method, the normal boundary intersection optimization method was applied to achieve an even spread of Pareto optimal solutions of the mean and variance equations of the weighted principal component; then, through the optimization of the mean and variance of the weighted principal component, the mean and variance of the original responses were also optimized. Moreover, confirmation runs were carried out to confirm the process robustness regarding the noise factor, tool overhang length.

In relation to cutting forces modeling, besides presenting multivariate and univariate cutting force models for mean and variance in the tool coordinate system, the present paper presents cutting force models for mean and variance equations in the workpiece coordinate system in the time domain. These models are also robust regarding the tool overhang length variation.

To allow robust design and optimization, the tool overhang length (l_{to}) was considered as noise factor because in cavity machining, there are specific workpiece geometries that constrain the tool overhang length [24]. Then, it is not a control factor, i.e., it does not depend on the experimenter choice. Figure 2a illustrates a mold with hole-making tasks, while Fig. 2b shows that if l_{to} is not enough, the tool holder may
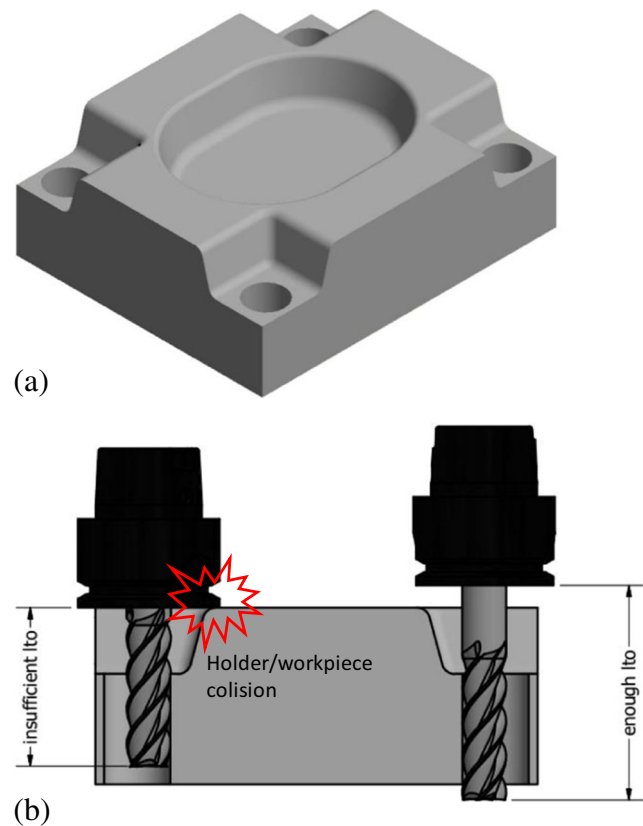

(a)

(b)

Fig. 2 **a** Mold with hole-making tasks. **b** Insufficient × enough tool overhang length (l_{to}) for the helical milling

collide with the workpiece during the helical milling process. There are several papers dealing with l_{to} effect, modeling, and optimization in machining processes [25–27]. Quantifying the effect of l_{to} on process responses is important, but minimizing its effect on process performance is essential because sometimes, the tool overhang length must be set according to the workpiece geometry. It is necessary to select optimal process factor levels to optimize the multiple set of responses, making the process robust with consideration to the tool overhang length variation. To achieve this aim, l_{to} was controlled at the experimental phase to assure the cutting force robustness regarding its variation in a practical situation.

The relevance of the present paper to industrial problems and situations is related to the fact that in on-line optimization situations, engineers deal with environmental factors and correlated process outcomes. In relation to process application, the helical milling brings a contribution in cutting forces modeling, considering the robustness regarding the tool overhang length variation, providing cutting force models in the tool and workpiece coordinate systems. Firstly, regarding noise factors, they are present in distinct manufacturing systems and are always referred as sources of errors that may not be easily controlled, leading to quality characteristic levels frequently outside upper and lower process control limits. Secondly, regarding correlated process outcomes, they may

impact negatively the process of evaluating regression coefficients, leading to predicting models that do not correctly represent real process performances. Therefore, the MMSE$_W$-NBI modeling and optimization method can easily take part of engineer's routine to deal with industrial problems related to optimization issues that contemplate environmental factors and correlated outcomes since the multivariate robust modeling and optimization method combines techniques capable of overcoming the aforementioned issues.

2 Robust parameter design

Robust parameter design (RPD) is a methodology to improve the quality of a product by minimizing the effect of causes of variation without eliminating them. This is achieved by optimizing process making its performance minimally sensitive to causes of variation [28]. RPD through response surface methodology (RSM) was firstly proposed by Myers et al. [29] with the purpose of modeling the mean and variance equations separately. In the context of RPD, different RSM approaches are available and the two most popular are crossed arrays and combined arrays. Crossed array is the first RPD methodology and is made up of an inner array, considering controllable factors, and an outer orthogonal array containing noise factors. This methodology, however, does not consider the interactions between process and noise factors and requires a considerable number of runs [30].

Combined arrays were proposed by Welch et al. and Shoemaker et al. [31, 32] and consist of running an experimental design containing both controllable and noise factors, eliminating the axial points related to noise factors as suggested by Myers et al. [29]. Taking into consideration controllable and noise factors into a single design leads to lower number of experimental runs and allows estimating the interaction between them [29, 31–33].

Through a combined array based on a central composite design (CCD), a surface response model for the quality characteristics, in function of controllable and noise factors, $y(\mathbf{x},\mathbf{z})$, can be obtained using ordinal or weighted least squares, OLS and WLS, respectively. Equation (7) presents the full quadratic response surface model, where x and z are the vectors of controllable and noise factors, respectively. $1 \le i \le k$ and $1 \le j \le r$, where k is the number of controllable factors and r is the number of noise factors. β, λ, and δ are coefficients of the quadratic model.

$$y(\mathbf{x},\mathbf{z}) = \beta_0 + \sum_{i=1}^{k} \beta_i x_i + \sum_{i=1}^{k} \beta_{ii} x_i^2 + \sum_{i<j} \sum \beta_{ij} x_i x_j \tag{7}$$

$$+ \sum_{j=1}^{r} \lambda_j z_j + \sum_{i=1}^{k} \sum_{j=1}^{r} \delta_{ij} x_i z_j + \varepsilon$$

Assuming independent noise factors with mean error equals to zero, variance $\sigma_{z_j}^2$, and that noise factors are uncorrelated with the random error ε, the mean and variance equations can be obtained in Eq. (8) and Eq. (9), respectively. $\sigma_{z_j}^2$ can be considered equal to 1 since the factor levels are scaled, and σ^2 is the residual error obtained in ANOVA. This approach is referred to as the propagation of error (POE). The variance equation is essentially a response surface with linear, quadratic, and second-order interaction terms.

$$E_z[y(\mathbf{x},\mathbf{z})] = f(\mathbf{x}) = \beta_0 + \sum_{i=1}^{k} \beta_i x_i + \sum_{i=1}^{k} \beta_{ii} x_i^2 + \sum_{i<j} \sum \beta_{ij} x_i x_j \tag{8}$$

$$V_z[y(\mathbf{x},\mathbf{z})] = \sigma_{z_j}^2 \left\{ \sum_{j=1}^{r} \left[\frac{\partial y(\mathbf{x},\mathbf{z})}{\partial z_j} \right]^2 \right\} + \sigma^2 \tag{9}$$

3 Mean square error optimization

The mean square error (MSE) optimization method was proposed by Box [34] and studied by Lin and Tu [35] and is expressed in Eq. (10), where T is the Utopia point obtained by $\text{Min}_{\mathbf{x} \in \Omega}[\hat{y}(\mathbf{x})]$, $\hat{y}(\mathbf{x})$ corresponds to the mean equation and $\hat{\sigma}^2$ is the variance equation. This approach, according to the authors, aims to minimize bias and variance and may be called dual response surface (DRS). Furthermore, mean and variance models can be obtained using crossed array or combined array approaches.

$$\text{Min} \left\{ \text{MSE} = \left(\hat{y} - T \right)^2 + \hat{\sigma}^2 \right\} \tag{10}$$

Lin and Tu [35] also proposed the weighting of the mean and variance equations, as in Eq. (11), in order to allow the evaluation of various operational settings based on w_1 and w_2 values of interest.

$$\text{Min} \left\{ \text{MSE}_w = w_1 \left(\hat{y} - T \right)^2 + w_2 \hat{\sigma}^2 \right\} \tag{11}$$

In a scenario considering multiple modeled DRS, the optimization problem has multivariate nature and consists of a multivariate mean square error optimization. Thereby, Köksoy [36] extended the MSE criteria, proposing an agglutination strategy that optimizes the MSE of multiple responses, using a weighted sum or choosing the more important MSE function as objective function and setting the others as constraints. The agglutination strategy using weighted sum is exposed in Eq. (12).

$$\text{Min} \left\{ \text{MSE}_T = \sum_{i=1}^{p} w_i \text{MSE}_i \right\} \tag{12}$$

Since most of manufacturing processes present multivariate nature, with significant correlation structure among responses, Paiva et al. [37] proposed a combination of MSE concepts with surface responses wrote in terms of principal component scores. This approach is the multivariate mean square error (MMSE), as illustrated in Eq. (13).

$$\text{Min}\left\{MMSE_i = \left[\left(PC_i - \xi_{PC_i}\right)^2 + \lambda_i\right]\right\} \tag{13}$$

In Eq. (13), PC_i is the regression model for the i-th principal component score, ξ_{PC_i} is the Utopia point for this score, and λ_i is its respective eigenvalue. For p correlated responses, there are p uncorrelated principal component scores; thereby, the MMSE approach could be expanded considering the k most representative scores of data variability, i.e., scores with $\lambda_i \geq 1$. Equation (14) expresses this agglutination.

$$
\begin{aligned}
\text{Min } MMSE_\text{T} &= \left[\prod_{i=1}^{k}\left(MMSE_i | \lambda_i \geq 1\right)\right]^{\left(\frac{1}{k}\right)} \\
&= \left\{\prod_{i=1}^{k}\left[\left(PC_i - \xi_{PC_i}\right)^2 + \lambda_i | \lambda_i \geq 1\right]\right\}^{\left(\frac{1}{k}\right)} \\
i &= 1, 2, \ldots, k; \quad k \leq p
\end{aligned} \tag{14}
$$

Paiva et al. [38] applied $MMSE_\text{T}$ on RPD considering a crossed array. Subsequently, Paiva et al. [39] extended the referred multivariate methodology for RPD considering a combined array. Through p correlated response models, considering process and noise factors, response models for the most representative principal component scores were achieved. Appling the POE approach, mean and variance equations for principal components were obtained and this multivariate optimization approach is exposed in Eq. (15).

$$\text{Min } MMSE(F_i)(\mathbf{x}) = \left\{\prod_{i=1}^{k}\left[\omega\left(E_z\left[P_c(\mathbf{x}, \mathbf{z})_i\right] - \xi_{PC_{z_i}}\right)^2 + (1-\omega)\left[\sigma_z^2 \sum_{j=1}^{r}\left(\frac{\partial P_c(\mathbf{x}, \mathbf{z})_i}{\partial z_j}\right) + \sigma^2\right]\right]\right\}^{\left(\frac{1}{k}\right)} \tag{15}$$
$$i = 1, 2, \ldots, k; \quad k \leq p$$

4 Weighted principal component analysis

In analyzing multi-response data, serious mistakes can be made. Fitting multi-response models without taking into consideration dependencies among responses can lead to difficulties, and the validity of the regression models under study may be denied [40]. Principal component analysis (PCA) may be applied to describe correlated responses in terms of uncorrelated principal components and to reduce problem dimension [41]. In the current context, an alternative approach for the multivariate mean square error optimization may consider all the p principal component scores agglomerated into a single score weighted by their respective eigenvalues. The weighted principal component (WPC) resumes all p components into one component without any loss of information [42], simplifying the modeling and optimization.

The main idea behind the principal component analysis is to reduce the p original dimension in a system of $k \leq p$ coordinates considering a significant part of the correlated response information. Considering p correlated responses $\mathbf{y}^T = \left[y_1, \ y_2, \ \ldots, \ y_p\right]$, with mean vector $\boldsymbol{\mu}^T = [\mu_1, \ \mu_2, \ \ldots, \ \mu_p]$ and variance–covariance matrix Σ_{pxp}, p uncorrelated principal components can be achieved with the maximization of the variance of the linear combination

$PC_i = \mathbf{e}_i^T \mathbf{y} = e_{1i}y_1 + e_{2i}y_2 + \ldots + e_{pi}y_p$, with $i = 1, 2, \ldots, p$, where $\mathbf{e}_i^T$ represents the standardized eigenvectors obtained from the eigenvalues, $\lambda_1 \geq \lambda_2 \geq \ldots \geq 0$, and from the variance–covariance matrix Σ_{pxp} [43]. These linear combinations describe the selection of a new coordinate system obtained by rotating the original system [44].

In a real situation, it is not possible to know the population parameters, and the responses may present different scales and units. Considering the estimated mean vector $\bar{\mathbf{y}}^T = \left[\bar{y}_1, \ \bar{y}_2, \ \ldots, \ \bar{y}_p\right]$ and the estimated correlation matrix $\mathbf{R}$, the i-th principal component estimation is defined as $\hat{PC}_i = [\mathbf{Z}]^T[\mathbf{E}]$, where $\mathbf{Z}$ is the standardized original responses matrix and $\mathbf{E}$ is the eigenvectors matrix. In this scenario, the exposed principles can be used to obtain the principal component estimates.

The weighted principal component score WPC is the linear combination of scores of the p principal components, which considers its respective eigenvalues as scalars [42], as exposed in Eq. (16), in which the subscript "s" means the experimental run number.

$$WPC_s = \hat{\lambda}_1 \hat{PC}_{1s} + \hat{\lambda}_2 \hat{PC}_{2s} + \ldots + \hat{\lambda}_r \hat{PC}_{rs} \tag{16}$$

5 Normal boundary intersection method

To overcome the drawbacks of the weighted sum method, Das and Dennis [45] proposed an approach called normal boundary intersection (NBI), which is a geometrically inspired scalarization method for solving non-linear multi-objective optimization problems, and its aim is to obtain evenly distributed Pareto optimal points, generating continuous frontiers regardless the weights attributed to the objective functions, which are process responses. In contrast to the weighted sum method, the NBI method finds a near-uniform spread of Pareto optimal solution options in the frontier [46]. In accordance with Zhang et al. [47], a set of points can be only considered as Pareto optimal if any improvement in one of the process responses leads to a setback in at least one of the other responses. Thus, the NBI method allows the experimenter a better exploitation of process parameters, facilitating analyses of the trade-off between a set of process responses.

The first step of the NBI method is to establish the payoff matrix Φ [48, 49]. The payoff matrix is composed by the individual optimization of each objective function, evaluated in all objective functions involved in the multi-objective optimization problem. The payoff matrix can be written as in Eq. (17).

$$\Phi = \begin{bmatrix} f_1^*(\mathbf{x}_1^*) & \cdots & f_1(\mathbf{x}_i^*) & \cdots & f_1(\mathbf{x}_m^*) \\ \vdots & \ddots & & & \vdots \\ f_i(\mathbf{x}_1^*) & \cdots & f_i^*(\mathbf{x}_i^*) & \cdots & f_i(\mathbf{x}_m^*) \\ \vdots & & & \ddots & \vdots \\ f_m(\mathbf{x}_1^*) & \cdots & f_m(\mathbf{x}_i^*) & \cdots & f_m^*(\mathbf{x}_m^*) \end{bmatrix} \quad (17)$$

In Φ, $\mathbf{x}_i^*$ represents a solution vector composed by values of process parameters that minimizes the i-th objective function f_i individually. Thus, $f_i^*(\mathbf{x}_i^*)$ is the optimal solution for the i-th objective function, $i = 1, 2, \ldots, m$. The other solutions $f_i(\mathbf{x}_i^*)$, which are not on the main diagonal of Φ, are obtained by replacing $\mathbf{x}_i^*$ in the remaining functions.

The set of individual optimal solutions that represents the main diagonal forms a vector called Utopia point, $f^U = \left[f_1^*(\mathbf{x}_1^*), \ldots, f_i^*(\mathbf{x}_i^*), \ldots, f_m^*(\mathbf{x}_m^*) \right]^T$. On the other hand, the set of solutions that are most distant from the individual optimal of each objective function, i.e., $\mathrm{Max}\left\{ f_i^*(\mathbf{x}_i^*), \ldots, f_i(\mathbf{x}_m^*) \right\}$, forms a vector known as pseudo nadir point, $f^{PN} = \left[f_1^{PN}, \ldots, f_i^{PN}, \ldots, f_m^{PN} \right]^T$. The normalization of each objective function should be made due to the nature of each process response. In doing so, the objective functions become dimensionless. Normalization can be performed as in Eq. (18).

$$\overline{f}_i(\mathbf{x}) = \frac{f_i(\mathbf{x}) - f_i^*}{f_i^{PN} - f_i^*} \quad (18)$$

The normalized payoff matrix $\overline{\Phi}$ is in Eq. (19).

$$\overline{\Phi} = \begin{bmatrix} \overline{f}_1(\mathbf{x}_1^*) & \cdots & \overline{f}_1(\mathbf{x}_i^*) & \cdots & \overline{f}_1(\mathbf{x}_m^*) \\ \vdots & \ddots & & & \vdots \\ \overline{f}_i(\mathbf{x}_1^*) & \cdots & \overline{f}_i(\mathbf{x}_i^*) & \cdots & \overline{f}_i(\mathbf{x}_m^*) \\ \vdots & & & \ddots & \vdots \\ \overline{f}_m(\mathbf{x}_1^*) & \cdots & \overline{f}_m(\mathbf{x}_i^*) & \cdots & \overline{f}_m(\mathbf{x}_m^*) \end{bmatrix} \quad (19)$$

According to Das and Dennis [45], the convex combinations formed by the sets of points of each row of $\overline{\Phi}$ generate the convex hull of individual minima (CHIM), or Utopia line in bi-objective problems or Utopia plan in situations with more than two objective functions [46]. The Utopia line/plan is delimited by anchor points. An anchor point is the result of the individual optimization of only one objective function [46].

An optimization problem based on the NBI method can be written as in Eq. (20) [45].

$$
\begin{aligned}
&\mathrm{Max}_{(\mathbf{x},t)} \quad && t \\
&Subject\ to: \quad && \overline{\Phi}\beta + t\hat{\mathbf{n}} = \overline{\mathbf{F}}(\mathbf{x}) \\
& && \mathbf{x} \in \Omega \\
& && g_j(\mathbf{x}) \leq 0 \\
& && h_j(\mathbf{x}) = 0
\end{aligned} \quad (20)
$$

Where $t \in R$ represents the distance between a point on CHIM and a point on the Pareto frontier and $\hat{\mathbf{n}}$ represents a unit vector normal to CHIM towards the origin that crosses a point $\overline{\Phi}\beta_i$. The weight β is a vector containing the degree of importance that is intended to be linked to each objective function, $\beta = [\beta_1, \ldots, \beta_i, \ldots, \beta_m]^T$, $0 \leq \beta_i \leq 1$, $\sum_{i=1}^{m}\beta_i = 1$, $i = 1, 2, \ldots, m$. $\overline{\mathbf{F}}(\mathbf{x})$ is a vector containing the normalized objective functions, $\overline{\mathbf{F}}(\mathbf{x}) = \left[\overline{f}_1(\mathbf{x}^*), \ldots, \overline{f}_i(\mathbf{x}^*), \ldots, \overline{f}_m(\mathbf{x}^*) \right]^T$. Thus, $\overline{\Phi}\beta + t\hat{\mathbf{n}}$ represents a set of points normal to CHIM. According to Das and Dennis [50], the point of intersection between the normal $\overline{\Phi}\beta + t\hat{\mathbf{n}}$ and the boundary of the feasible region (Pareto frontier) closest to the origin is the global optimum. This global optimum will correspond to the maximization of the distance between a point on CHIM and the Pareto frontier.

6 Multivariate robust parameter design through weighted principal component analysis and normal boundary intersection

It is possible to obtain a response model considering the weighted principal component scores WPC_s by defining an experimental procedure based on a central composite design,

which combines the process and noise factors. The response model is shown in Eq. (21).

$$
WPC(\mathbf{x}, \mathbf{z}) = \beta_0 + \sum_{i=1}^{k} \beta_i x_i + \sum_{i=1}^{k} \beta_{ii} x_i^2 + \sum_{i<j} \sum \beta_{ij} x_i x_j \quad (21)
$$
$$
+ \sum_{j=1}^{k} \lambda_j z_j + \sum_{i=1}^{k} \sum_{j=1}^{r} \delta_{ij} x_i z_j + \varepsilon
$$

Based on POE principles, mean and variance equations can be obtained for WPC, through Eq. (22) and Eq. (23). These equations represent, respectively, the multivariate mean and variance of the p correlated responses.

$$
E_z[WPC(\mathbf{x}, \mathbf{z})] = E_z(\mathbf{x}) \quad (22)
$$

$$
V_z[WPC(\mathbf{x}, \mathbf{z})] = V_z(\mathbf{x}) = \sigma_{z_j}^2 \left\{ \sum_{j=1}^{r} \left[\frac{\partial WPC(\mathbf{x}, \mathbf{z})}{\partial z_j} \right]^2 \right\} + \sigma^2 \quad (23)
$$

By using Eq. (22) and Eq. (23), a multivariate mean square error criterion based on the weighted principal component scores may be presented, as in Eq. (24). The constraint $\mathbf{x}^T\mathbf{x} \leq \rho^2$ is related to the experimental region, ξ_{WPCz} is the Utopia point of $E_z[WPC(\mathbf{x}, \mathbf{z})]$ obtained by $Min_{\mathbf{x} \in \Omega}\{E_z[WPC(\mathbf{x}, \mathbf{z})]\}$. Through this approach, the multivariate bias and variance can be minimized.

$$
Min\ MMSE_W = \left\{ \omega\left(E_z[WPC(\mathbf{x}, \mathbf{z})] - \xi_{WPCz}\right)^2 + (1-\omega)\left[\sigma_{z_j}^2 \sum_{j=1}^{r} \left(\frac{\partial WPC(\mathbf{x}, \mathbf{z})}{\partial z_j}\right)^2 + \sigma^2\right]\right\} \quad (24)
$$
$$
subject\quad to: \mathbf{x}^T\mathbf{x} \leq \rho^2
$$

Paiva et al. [51] applied similar criteria in modeling a response surface for WPC considering only controllable factors. This approach presents a robust optimization $MMSE_W$ considering WPC modeling based on combined arrays and on the POE approach to derive mean and variance equations. The $MMSE_W$ proposed approach in Eq. (24) can be used to generate trade-off solutions for the mean and variance dual optimization problem. However, this approach is a weighted sum of mean and variance as well as the approaches in Eqs. 10–15.

Due to the shortcomings of the weighted sum method in generating an even spread of Pareto optimal points, the NBI method may be applied together with the $MMSE_W$ method, depicted in Eq. (24). Considering the bi-objective NBI problem applied to the trade-off problem between Eq. (22) and Eq. (23), a payoff matrix Φ is initially constructed based on optimal points of each isolated objective function. The solutions that minimize $E_z(\mathbf{x})$ and $V_z(\mathbf{x})$ are, respectively, $\mathbf{x}_E^*$ and $\mathbf{x}_V^*$. The pay-off matrix for this specific dual problem is in Eq. (25).

$$
\Phi = \begin{bmatrix} E_z^*(\mathbf{x}_E^*) & E_z^{PN}(\mathbf{x}_V^*) \\ V_z^{PN}(\mathbf{x}_E^*) & V_z^*(\mathbf{x}_V^*) \end{bmatrix} \quad (25)
$$

The elements of the payoff matrix will compose the anchor points, i.e., the extreme values of the Pareto frontier. $E_z^*(\mathbf{x}_E^*)$ and $V_z^*(\mathbf{x}_V^*)$ are utopia points, i.e., optimal values obtained through the optimization of $E_z(\mathbf{x})$ and $V_z(\mathbf{x})$, respectively. The worst results for these functions are called pseudo nadir points and are labeled $E_z^{PN}(\mathbf{x}_V^*)$ and $V_z^{PN}(\mathbf{x}_E^*)$. These extreme values on the solution space can be used to normalize the objective functions, as expressed in Eq. (26) and Eq. (27).

$$
\overline{E}_z(\mathbf{x}) = \frac{E_z(\mathbf{x}) - E_z^*(\mathbf{x}_E^*)}{E_z^{PN}(\mathbf{x}_V^*) - E_z^*(\mathbf{x}_E^*)} \quad (26)
$$

$$
\overline{V}_z(\mathbf{x}) = \frac{V_z(\mathbf{x}) - V_z^*(\mathbf{x}_V^*)}{V_z^{PN}(\mathbf{x}_E^*) - V_z^*(\mathbf{x}_V^*)} \quad (27)
$$

Finally, the solution for this two-objective NBI optimization problem, called $MMSE_W$-NBI, can be exposed as in Eq. (28).

$$
\begin{aligned} &Min\ \overline{E}_z(\mathbf{x}) \\ &s.t.: \overline{E}_z(\mathbf{x}) - \overline{V}_z(\mathbf{x}) + 2w_i - 1 = 0 \\ &g_j(\mathbf{x}) \geq 0 \\ &0 \leq \omega_i \leq 1 \end{aligned} \quad (28)
$$

The $MMSE_W$-NBI problem needs to be solved iteratively considering different weights. The space between two consecutive weights is defined as a constant δ [52]. For a bi-objective case, the number of Pareto optimal solutions (n) may be calculated as $n = \delta^{-1} + 1$. Thus, it is possible to obtain weights for the optimization problem presented in Eq. (29) as $w_i = (i-1)\delta$, $i = 1, 2, \ldots, n$. Therefore, $w_1 = 0$, $w_2 = \delta$, $w_2 = \delta$, $\ldots$, $w_n = 1$.

Explicitly, the $MMSE_W$-NBI method, proposed in this paper, in terms of mean and variance of the weighted principal component, Eq. (29), allows obtaining equispaced Pareto frontiers, considering the mean and variance equations of the WPC response model, which represents a set of correlated

responses without loss of information. In Eq. (29), the symbol ψ indicates that the value of the variance equation between brackets is in the normalized form.

$$\text{Min } \overline{E}_z[\text{WPC}(\mathbf{x}, \mathbf{z})]$$
$$s.t. : \overline{E}_z[\text{WPC}(\mathbf{x}, \mathbf{z})] - \left[\sigma_{z_j}^2 \sum_{j=1}^{r} \left(\frac{\partial \text{WPC}(\mathbf{x}, \mathbf{z})}{\partial z_j}\right)^2 + \sigma^2\right]^{\psi} + 2w_i - 1 = 0 \quad (29)$$
$$\mathbf{x}^{\mathbf{T}}\mathbf{x} \leq \rho^2$$
$$0 \leq w_i \leq 1$$

The MMSE$_W$-NBI method may be referred as a new procedure to optimize bias and variance of multivariate data without loss of information. The bias $\omega(E_z[\text{WPC}(\mathbf{x}, \mathbf{z})] - \xi_{\text{WPCz}})^2$ is not optimized explicitly in the objective function of the formulation in Eq. (29). Nevertheless, as the target ξ_{WPCz} is obtained through $\text{Min}_{\mathbf{x} \in \Omega}\{E_z[\text{WPC}(\mathbf{x}, \mathbf{z})]\}$, the proposed method in Eq. (29) will naturally minimize the bias and may be considered an alternative to the multivariate robust mean square error optimization to achieve an even spread of solutions for the trade-off between mean and variance of multivariate data without loss of information.

Lopes et al. [53] proposed a similar approach for robust modeling and optimization of the arithmetic average surface roughness and the maximum roughness height. However, the present paper proposes to the experimenter the possibility of using the weighted principal component technique, avoiding loss of information, i.e., 100% of the variance–covariance structure of the original set of process outcomes is taken into consideration to estimate regression coefficients that consider all the variance–covariance influence on the response surface models. Besides that, applying the MMSE$_W$-NBI method on the helical milling is an important novelty since researches involving statistical influence of noise factors and correlated outcomes on this hole-making process have not been widely studied yet.

To solve the non-linear programming problems (NLP) proposed in Eq. (24) and Eq. (29), several algorithms can be applied. One alternative algorithm is the generalized reduced gradient (GRG) [38, 54].

To reach a robust approach to modeling and optimization of cutting forces in the helical milling process, the new proposed MMSE$_W$-NBI method is applied. The practical objective is to achieve cutting force models robust to the tool overhang length variation in the helical milling, i.e., in function of cutting parameters. Robustness is reached by achieving cutting parameter levels which are insensitive to the tool overhang length variation. This will allow a good fit of the cutting force models with experimental results in the tool and workpiece coordinate systems. The proposed approach is the first application of multivariate robust modeling and optimization in the helical milling process.

7 Experimental procedure

This work is a sequence of a previous work on modeling and optimization of the helical milling process of the aluminum alloy Al 7075 [55]. In this referred first work, three outcomes were considered: axial cutting force component (F_z), total roundness (Ron$_t$), and material removal rate (MRR). However, in this previous publication, only $F_z = F_a$ was presented with consideration to cutting force components. The radial cutting force F_r, measured in the xy plane, was not considered in that work since the intention was not only the modeling of cutting forces of the helical milling. In the present work, a statistically based approach is proposed for multivariate robust modeling and optimization of cutting forces of the helical milling process, without loss of information. When dealing with cutting forces modeling and optimization in the helical milling, it is important to consider F_a, which is related to the axial direction and is generally the main cutting force component in terms of magnitude, and F_r, which is measured in the circular plane, and consequently may be related to dimensional and geometrical deviations. Besides considering the cutting force components in the tool coordinate system, i.e., F_a and F_r, the present approach provides models for the cutting force components in the workpiece coordinate system F_x, F_y, and F_z. In these two viewpoints, robust models are provided, mean and variance models, considering the propagation of error regarding the tool overhang length.

F_a and F_r were modeled in function of three controllable variables (CV) and one noise variable (NV) that can be seen in Table 1 along with their symbols, units, and levels. The tool overhang length was chosen as noise variable because it can be controlled only in an experimental scenario; on the other hand, it cannot be controlled at a production scenario since in molds and die machining there are workpieces geometries which constrain the tool overhang length, to avoid collisions between tool system and workpiece/fixture. Figure 3 illustrates the setup of the three tool overhang length levels. Consequently, the RPD-RSM methodology is applied in this work to make F_a and F_r less sensitive to the tool overhang length variation. It is important to study the robustness of the tool overhang length in relation to cutting forces in helical milling, especially regarding F_r, since the tool overhang length is related to tool deflection, which may cause vibrations, and consequently dimensional, geometrical, and microgeometrical errors [17]. Moreover, the variables presented in Table 1 were also taken into consideration to model F_r and the mean and variance equations of the weighted principal component.

With the variables and levels presented in Table 1, a central composite design with 26 runs was used. Then, $n_F = 2^{k+r} = 2^{3+1} = 16$ factorial points (coded level = ± 1) were carried out taking into consideration controllable and noise variables. The factorial points are important to study main effects of process and factors and process × process and process × noise

Table 1 Controllable and noise variables. Adapted from [55] with permission from Elsevier, license number 4153600491710

Type of variables	Variables	Symbols	Units	Levels				
				−2	−1	0	1	2
CV	Axial feed per tooth	f_{za}	μm/tooth	0.5	4	7.5	11	14.5
CV	Tangential feed per tooth	f_{zt}	μm/tooth	15	40	65	90	115
CV	Cutting velocity	v_c	m/min	10	30	50	70	90
NV	Tool overhang length	l_{to}	mm	–	30	38	46	–

interactions. The propagation of error considers not only the isolated effect of noise variable but also the effect of noise on controllable variables. $n_A = 2 \times k = 2 \times 3 = 6$ axial points (coded levels $= \pm 2$) were conducted considering only process variables to estimate their quadratic effects. Finally, $n_C = 4$ center points (coded level $= 0$) were conducted to allow an independent estimation of experimental error and support the calculation of quadratic terms.

The axial runs corresponding to the tool overhang length (noise variable) were not considered, and the experiments were conducted in random order to yield the most accurate analyses of data.

The axial distance for this design is $\rho = (2^4)^{1/4} = 2$. However, when considering the process experimental space, since mean and variance equations are in function of only controllable parameters, the axial distance will become $\rho = (2^3)^{1/4} = 1.682$, which is the radius of the spherical constraint to the controllable variables in the optimization problem; thus, the solutions will be forced by the spherical constraint to fall within the experimental solution.

Here, besides F_a, F_r was calculated considering the results of F_x and F_y. Since F_a and F_r are statically correlated, the new non-linear multivariate robust modeling and optimization method (MMSE$_W$-NBI) can be performed to optimize both responses through the optimization of mean and variance equations of the weighted principal component, $E_z[WPC(\mathbf{x}, \mathbf{z})]$ and $V_z[WPC(\mathbf{x}, \mathbf{z})]$, respectively, without loss of information.

A CNC machining center was used in the experimental tests, with the following characteristics: *Romi Discovery 560*, maximum power of 15 kW, spindle speed of 10,000 RPM, numerical control *Siemens* 810D CNC *Sinumerik*. The cutting tool used for machining the workpieces was an uncoated solid carbide end mill with the following characteristics: 10 mm diameter, 4 teeth, and 30° helix angle. The cutting fluid was soluble biodegradable emulsifiable oil for machining Bio 100 from *Biolub Química*® applied on wet condition.

The characteristics of the aluminum alloy Al 7075 workpieces were 23-mm diameter and 14-mm height. Boreholes with 15-mm diameter were obtained in helical milling tests. Due to the ratio between mechanical resistance and density, the aluminum alloy Al 7075 has been widely applied in the aircraft industry due to its high mechanical strength to specific mass.

The machining components F_a and F_r were measured with a stationary piezoelectric dynamometer, model *Kistler®9272* with four components and signal amplifier. The three components F_x, F_y, and F_z in the workpiece coordinate system were measured during the tests. Figure 4 shows the experimental setup (a), helical milling test (b), nomenclature (c), and graphical results of cutting forces (d).

In this paper, the following software were used for modeling and optimization: MS-Excel®, Minitab®, and

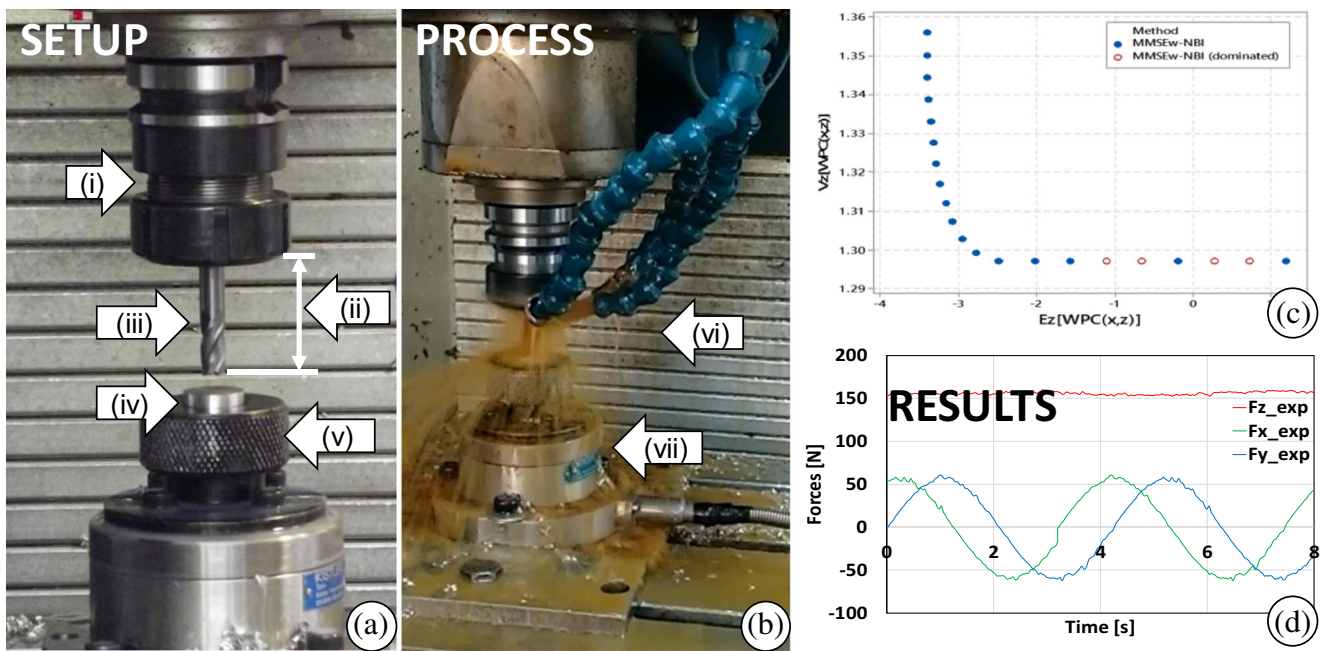**Fig. 3** Tool overhang length setup
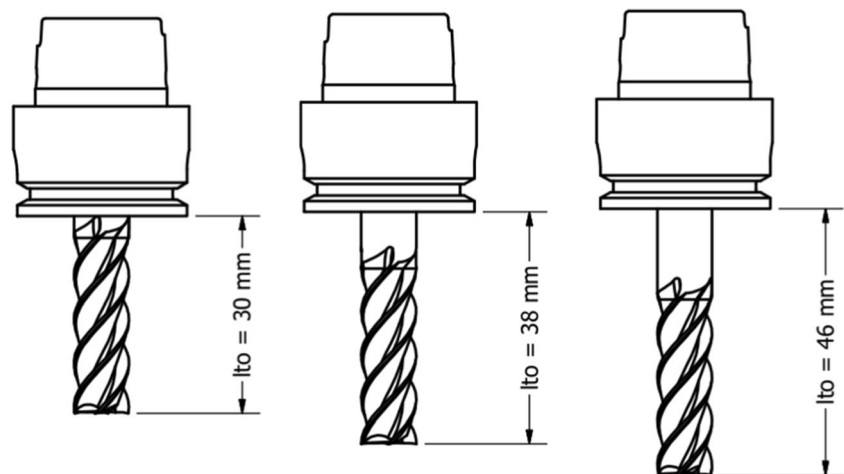
Fig. 4 Experimental procedure (i) holder, (ii) tool overhang length, (iii) tool, (iv) workpiece, (v) fixture, (vi) hole-making through helical milling, (vii) dynamometer

Matlab®. The routine of the MMSE$_W$-NBI method is illustrated in Fig. 5. In Fig. 5, it is seen that if there is no correlation among outcomes, univariate analysis should be performed and an optimization method should be chosen to solve the non-linear optimization problem; this process is illustrated by the symbol (+), indicating that this is another process.

Considering Fig. 5, the procedure for the MMSE$_W$-NBI method can be described for replication and better understanding through the following steps:

Step 1: Define the experimental design
Define a central composite design combining control and noise factors. Run the experimental design, measure the responses and store the results.

Step 2: Evaluate the correlation among outcomes
Before starting PCA, it is indispensable to calculate the correlation among responses. It could be done by analyzing the Pearson correlation coefficient together with the *p value* for each pair of responses.

Step 3: Run the principal component analysis
In the case of correlation, run the PCA analysis for the correlated responses using the correlation matrix **R**. Store the scores of the p principal components and their respective eigenvalues and eigenvectors.

Step 4: Define the weighted principal component scores
Define the WPC scores as linear combinations of the scores of the p principal components weighted by their respective eigenvalues, as in Eq. (16). Store the WPC scores.

Step 5: Build the WPC response model in function of controllable and noise factors
Use ordinal (OLS) or weighted least square (WLS) methods to build a complete response model for WPC $(\mathbf{x}, \mathbf{z})$ through Eq. (21), considering linear terms, interaction between noise and control factors, and quadratic terms for controllable factors.

Step 6: Define mean and variance equations
Through RPD, define mean and variance equations of the weighted principal component, $E_z[\mathrm{WPC}(\mathbf{x}, \mathbf{z})]$ and $V_z[\mathrm{WPC}(\mathbf{x}, \mathbf{z})]$, respectively, as defined in Eq. (22) and Eq. (23). Henceforth, $E_z[\mathrm{WPC}(\mathbf{x}, \mathbf{z})]$ might be referenced as $E_z(\mathbf{x})$ and $V_z[\mathrm{WPC}(\mathbf{x}, \mathbf{z})]$ might be referenced as $V_z(\mathbf{x})$.

Step 7: Define the payoff matrix
Obtain the utopia points $E_z^*\left[\mathbf{x}_{E_z(\mathrm{WPC})}^*\right]$ and $V_z^*\left[\mathbf{x}_{V_z(\mathrm{WPC})}^*\right]$ through the constrained optimization problems $\mathrm{Min}_{\mathbf{x}^T\mathbf{x} \leq \rho^2}\{E_z[\mathrm{WPC}(\mathbf{x}, \mathbf{z})]\}$ and $\mathrm{Min}_{\mathbf{x}^T\mathbf{x} \leq \rho^2}\{V_z[\mathrm{WPC}(\mathbf{x}, \mathbf{z})]\}$, respectively. The solution vector $\mathbf{x}_{E_z(\mathrm{WPC})}^*$ corresponds to the best individual values of f_{za}, f_{zt}, and v_c that minimize $E_z(\mathbf{x}) = E_z[\mathrm{WPC}(\mathbf{x}, \mathbf{z})]$. In the same line of reasoning, $\mathbf{x}_{V_z(\mathrm{WPC})}^*$ contains the best individual values of the controllable variables that minimize $V_z(\mathbf{x}) = V_z[\mathrm{WPC}(\mathbf{x}, \mathbf{z})]$. Using $\mathbf{x}_{E_z(\mathrm{WPC})}^*$ and $\mathbf{x}_{V_z(\mathrm{WPC})}^*$, define the pseudo nadir points $E_z^{\mathrm{PN}}\left[\mathbf{x}_{V_z(\mathrm{WPC})}^*\right]$ and $V_z^{\mathrm{PN}}\left[\mathbf{x}_{E_z(\mathrm{WPC})}^*\right]$. Build the payoff matrix as in Eq. (25).
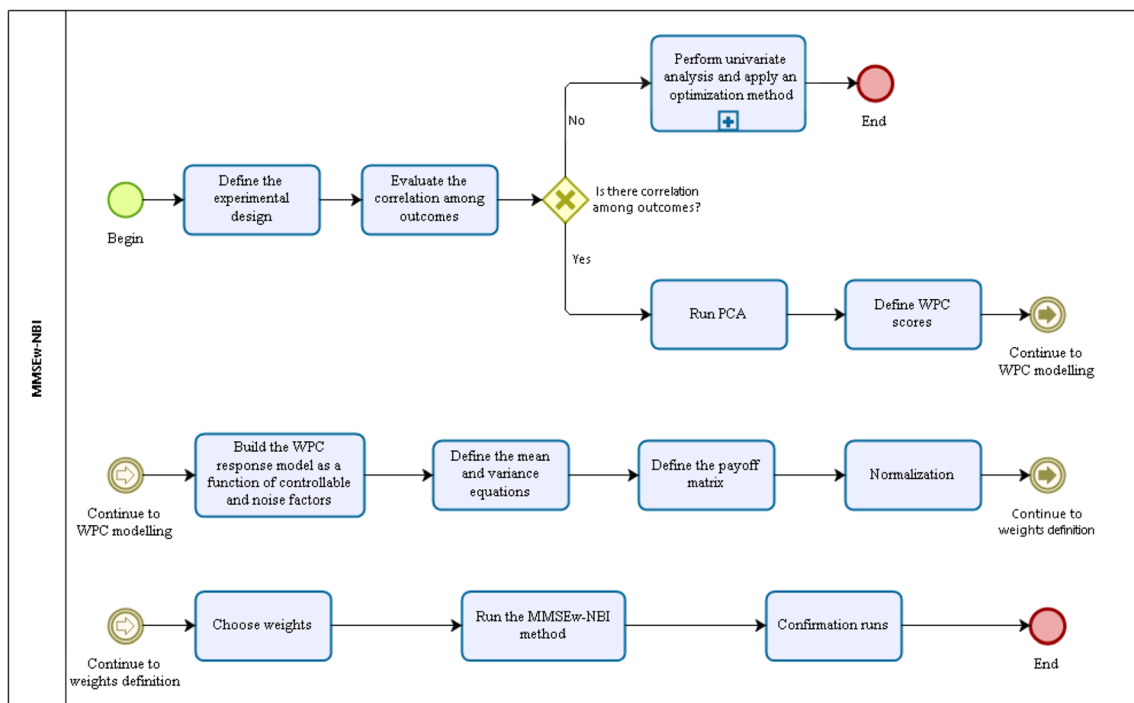
Step 8: Normalization

Fig. 5 Routine of the MMSE$_W$-NBI method

Using the payoff matrix, normalize the mean and variance functions of the weighted principal component as well as the payoff matrix, as proposed in Eq. (26) and Eq. (27).

Step 9: Choose weights

Before carrying out the MMSE$_W$-NBI method, the weights should be calculated. First, calculate the number of Pareto optimal solutions (n) according to the desired increment δ between weights. Given n and δ, it is possible to obtain weights w_i, which are in Eq. (29), as $w_i = (i - 1)\delta$, $i = 1, 2, \ldots, n$. For instance, in this paper, $w_n = 1$ forces the optimization problem to achieve the best setting of f_{za}, f_{zt}, and v_c inherent to the best level of $E_z[\text{WPC}(\mathbf{x},\mathbf{z})]$.

Step 10: Run the MMSE$_W$-NBI method

Solve the MMSE$_W$-NBI method iteratively for different weights, as defined in Eq. (29), using the GRG algorithm. Build a Pareto frontier with equispaced Pareto solutions considering the Pareto optimal points for $E_z(\mathbf{x}) = E_z[\text{WPC}(\mathbf{x}, \mathbf{z})]$ and $V_z(\mathbf{x}) = V_z[\text{WPC}(\mathbf{x}, \mathbf{z})]$.

Step 11: Confirmation runs

Choose one or more Pareto optimal points according to preferences of the decision maker. Run tests considering a robust optimal vector, for instance $\mathbf{x}_{w_i}^* = \left(f_{za}^*, f_{zt}^*, v_c^*\right)$, for different noise factor conditions. Test the process robustness for the Pareto optimal conditions and the proximity for the measured responses with the predicted values.

8 Results and discussion

8.1 Experimental design

Table 2 presents the experimental design with cutting force results for the helical milling tests in the aluminum alloy Al 7075. Here, in terms of experimental results, the novelty is the response F_r measured in the xy plane, which may cause dimensional, geometrical, and microgeometrical deviations. Besides, in the present approach, multivariate analysis is carried out, and cutting force models are obtained in the tool and workpiece coordinate system.

8.2 Correlation evaluation, principal component analysis, and weighted principal component scores estimation

The Pearson correlation coefficient between F_a and F_r was $r = 0.83$ with p value $= 0.000$, confirming a significant correlation between the responses at the significance level (α) of 0.05, and justifying the multivariate modeling. Considering the two responses, a spectral decomposition on the correlation matrix $\mathbf{R}$ can be performed to obtain eigenvalues and eigenvectors of $\mathbf{R}$. Thus, the results are stored in Table 3. The first principal component accounts for 91.6% of the variance–covariance structure between F_a and F_r, while the second one accounts for 8.4% of the data variability. It means that PC_1 could represent the original responses since it accounts for more than 80% of the

Table 2 Experimental design with responses. Adapted from [55] (experimental design and F_a) with permission from Elsevier, license number 4153600491710

Std order	CV			NV	Responses		Scores		
	f_{za} [μm/tooth]	f_{zt} [μm/tooth]	v_c [m/min]	l_{to} [mm]	F_a [N]	F_r [N]	PC$_1$ –	PC$_2$	WPC$_s$
1	4	40	30	30	147	136	−1.40	0.35	−2.51
2	11	40	30	30	249	248	0.99	0.10	1.83
3	4	90	30	30	184	113	−1.15	−0.35	−2.17
4	11	90	30	30	274	262	1.44	−0.09	2.63
5	4	40	70	30	186	136	−0.88	−0.16	−1.65
6	11	40	70	30	263	294	1.61	0.36	3.01
7	4	90	70	30	189	97	−1.23	−0.56	−2.35
8	11	90	70	30	272	232	1.14	−0.34	2.02
9	4	40	30	46	188	148	−0.75	−0.08	−1.39
10	11	40	30	46	266	284	1.55	0.22	2.87
11	4	90	30	46	215	97	−0.89	−0.90	−1.79
12	11	90	30	46	254	255	1.12	0.10	2.08
13	4	40	70	46	174	147	−0.94	0.10	−1.71
14	11	40	70	46	266	253	1.26	−0.07	2.29
15	4	90	70	46	198	91	−1.17	−0.74	−2.26
16	11	90	70	46	273	254	1.35	−0.15	2.45
17	0.5	65	50	38	30	25	−3.98	0.80	−7.15
18	14.5	65	50	38	288	346	2.43	0.54	4.53
19	7.5	15	50	38	176	190	−0.50	0.49	−0.83
20	7.5	115	50	38	194	179	−0.39	0.15	−0.68
21	7.5	65	10	38	171	202	−0.46	0.67	−0.72
22	7.5	65	90	38	197	196	−0.17	0.27	−0.26
23	7.5	65	50	38	228	187	0.14	−0.21	0.22
24	7.5	65	50	38	243	192	0.38	−0.35	0.63
25	7.5	65	50	38	227	202	0.26	−0.05	0.47
26	7.5	65	50	38	228	199	0.25	−0.09	0.44

variance–covariance structure and its eigenvalue is more than 1. However, a linear combination of both principal components may be calculated to avoid loss of information, leading to a representation of 100% of the variance–covariance structure besides solving the correlation issue. Therefore, the weighted principal component concept

Table 3 Eigenanalysis of F_a and F_r

	PC$_1$	PC$_2$
Eigenvalue	1.832	0.168
Proportion	0.916	0.084
Cumulative	0.916	1.000
Eigenvectors	PC$_1$	PC$_2$
F_a	0.707	−0.707
F_r	0.707	0.707

already stated in this work was considered for representing the uncorrelated components PC$_1$ and PC$_2$.

To illustrate the original responses and their principal components, Fig. 6 shows a scatter plot of the original responses correlated positively. Graphically, it can be illustrated in Fig. 6 what was stated in the previous paragraph in relation to the data variability explained by PC$_1$ and PC$_2$. In Fig. 6, it is seen that the variability explained by PC$_2$, inherent to the PC$_2$ axe, is lower than the variability explained by PC$_1$, inherent to PC$_1$ axe. Although PC$_1$ explains most of the variance–covariance structure, PC$_2$ should not be ignored when desiring to totally explain the variance–covariance structure inherent to F_a and F_r; therefore, it favors using the weighted principal component technique.

In Fig. 6, the ellipse is expressed by $(\mathbf{y}-\overline{\mathbf{y}})^T \mathbf{S}^{-1}(\mathbf{y}-\overline{\mathbf{y}}) = c^2$, where $\mathbf{y}^T = (F_a, F_r)$ is the vector of the original outcomes, $\overline{\mathbf{y}}^T = (\overline{F}_a;\ \overline{F}_r) = (214.61;\ 190.96)$, c is a constant and in this

Fig. 6 Correlated original responses ($r = 0.832$)
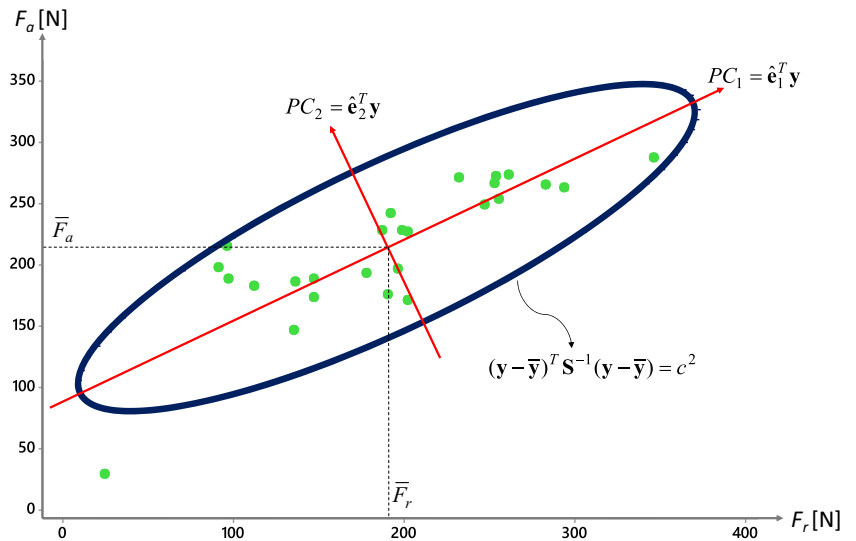
work $c^2 = 2.45$, which represents an ellipse at a confidence level of 95%, and

$$\mathbf{S} = \begin{bmatrix} 2998.57 & 3370.14 \\ 3370.14 & 5473.97 \end{bmatrix}$$

is the estimated variance–covariance matrix whose main diagonal contains the variances of F_a and F_r, and the secondary diagonal contains the covariance between F_a and F_r. There is a single point outside the confidence ellipse, which is correspondent to $F_a = 30$ N and $F_r = 25$ N, according to Table 2, row 17. In Fig. 7, it is seen that through the Mahalanobis distance approach, there is one outlier between the values of the outcomes F_a and F_r, and this outlier is related to the point outside the confidence ellipse in Fig. 6. This point is inherent to f_{za} set to 0.5 μm/tooth, which is its positive axial point. In the central composite design, the factorial and axial points are

at the same and highest distance from the center and, therefore, present the highest variance levels regarding the experimental region. As f_{za} is generally the most influent variable on cutting force components, this variability is expected in extreme points. To assure a balanced design and sufficient degrees of freedom, this point is important to estimate the quadratic effect of f_{za}.

The observed uncorrelation considering the new coordinate system with PC_1 and PC_2 axes is quite important for step 5 so that the coefficients of the WPC($\mathbf{x}, \mathbf{z}$) response surface model can be correctly estimated.

The scores of the weighted principal component, which represent the correlated responses without loss of information, were calculated through linear combination as in Eq. (16), considering the two principal component scores and their respective eigenvalues. The scores of the weighted principal component were stored in Table 2.

Fig. 7 Mahalanobis distance measures
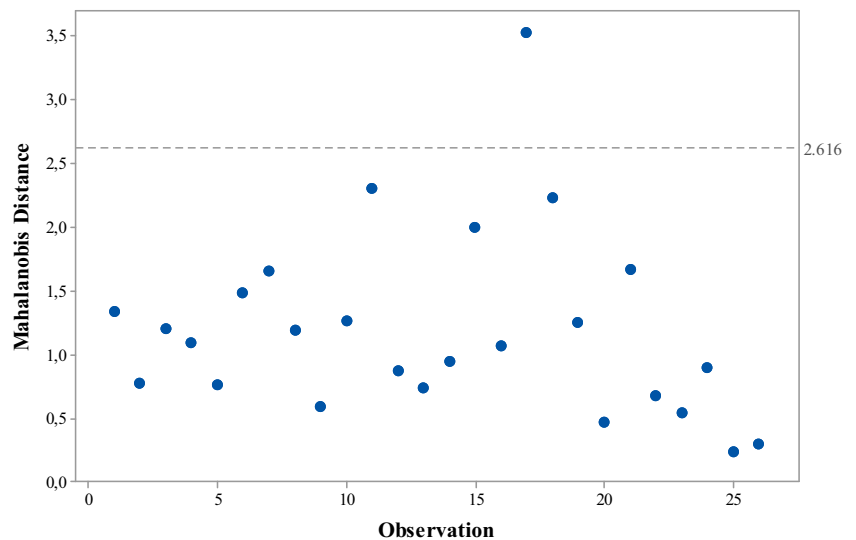
8.3 Response surface model and robust parameter design for weighted principal component, F_a, and F_r

Henceforth, the variables will be presented in coded units; therefore, the response surface models will be also presented in coded units unless it is written uncoded units. The full quadratic WPC($\mathbf{x}$,$\mathbf{z}$) response surface model proposed in Eq. (21) was calculated using the WLS algorithm and is expressed in Eq. (30). The full quadratic response surface models $F_a(\mathbf{x},\mathbf{z})$ and $F_r(\mathbf{x},\mathbf{z})$ were also calculated and are expressed in Eq. (31) and Eq. (32), respectively. The quadratic regression models represented by Eq. (31) and Eq.

(32) are essential to apply the Pareto optimal solutions considering the results of the MMSE_W-NBI optimization in the original responses. The statistical summary of the regression models, presented in Table 4, confirms good adjustments of data and no lack-of-fit (LOF) for all the full quadratic response surface models at the significance level of 0.05. The WPC($\mathbf{x}$,$\mathbf{z}$) model presented good determination coefficients, confirming high data variability explanation, with $R^2_{adj} = 95.11\%$, and suitable properties of prediction of the response model, $R^2_{pred} = 81.73\%$. Furthermore, the models of the original responses also presented good determination coefficients and properties of prediction.

$$\text{WPC}(\mathbf{x}, \mathbf{z}) = 0.605 + 2.231 f_{za} - 0.074 f_{zt} + 0.051 v_c + 0.100 l_{to} - 0.087 f_{za}^2 - 0.255 f_{zt}^2 - 0.193 v_c^2 + 0.053 f_{za} \times f_{zt} + 0.046 f_{za} \times v_c - 0.094 f_{za} \times l_{to} - 0.139 f_{zt} \times v_c - 0.055 f_{zt} \times l_{to} - 0.147 v_c \times l_{to} \tag{30}$$

$$F_a(\mathbf{x}, \mathbf{z}) = 242.575 + 43.100 f_{za} + 7.049 f_{zt} + 2.905 v_c + 5.151 l_{to} - 9.472 f_{za}^2 - 7.663 f_{zt}^2 - 7.882 v_c^2 - 6.001 f_{za} \times f_{zt} + 2.000 f_{za} \times v_c - 4.612 f_{za} \times l_{to} + 0.393 f_{zt} \times v_c - 3.480 f_{zt} \times l_{to} - 1.946 v_c \times l_{to} \tag{31}$$

$$F_r(\mathbf{x}, \mathbf{z}) = 194.422 + 72.028 f_{za} - 12.407 f_{zt} - 1.429 v_c + 1.787 l_{to} - 2.059 f_{za}^2 - 2.134 f_{zt}^2 + 1.205 v_c^2 + 7.009 f_{za} \times f_{zt} + 0.973 f_{za} \times v_c + 1.490 f_{za} \times l_{to} - 3.479 f_{zt} \times v_c - 3.223 f_{zt} \times l_{to} - 0.070 v_c \times l_{to} \tag{32}$$

Figure 8 shows interaction plots for WPC($\mathbf{x}$,$\mathbf{z}$). In these plots, process and noise effects on the cutting forces are illustrated. The positive effect of f_{za} on all the response surface models is remarkable. In this line of reasoning, the axial feed per tooth, which generates continuous cut, has a significant role on the cutting force levels.

The literature assures that the effect of f_{za} is positive and remarkable on the cutting force components because as f_{za} increases with f_{zt} kept unchanged, the axial cutting depth a_p^* increases, and both the areas that are cut by peripheral and frontal cutting edges increase. However, the low effect of f_{zt} was observed because when f_{zt} increases with f_{za} kept constant, the chip thickness in the peripheral cut increases, but the axial cutting depth a_p^* decreases [56].

The interaction plot between v_c and l_{to} shows that cutting velocity levels between 60 and 70 m/min are insensitive to tool overhang length variation. When performing the optimization, these levels of cutting velocity are confirmed. It means that with these levels of cutting velocity, the cutting force components will not vary due to the tool overhang length variation. Then, according to the geometry of the workpiece, the experimenter may set the necessary tool overhang length without affecting the cutting forces during helical milling.

As graphically illustrated, no significant linear effect is present regarding f_{zt} and v_c. However, some curvature may be observed in these parameters in relation to cutting forces. Besides, the slope difference in the interactions may guide the search for robustness. For instance, in the interaction between v_c and l_{to}, cutting velocity levels close to 60 m/min make the process robust to the tool overhang length variation. It means that with this cutting velocity, the cutting forces will not be affected by the variation of the tool overhang length.

Through the RPD approach, as proposed in Eq. (22) and Eq. (23), mean and variance equations were obtained in function of controllable variables, considering the variation transmitted by the noise factor. These models are robust to the tool overhang

Table 4 Model summary

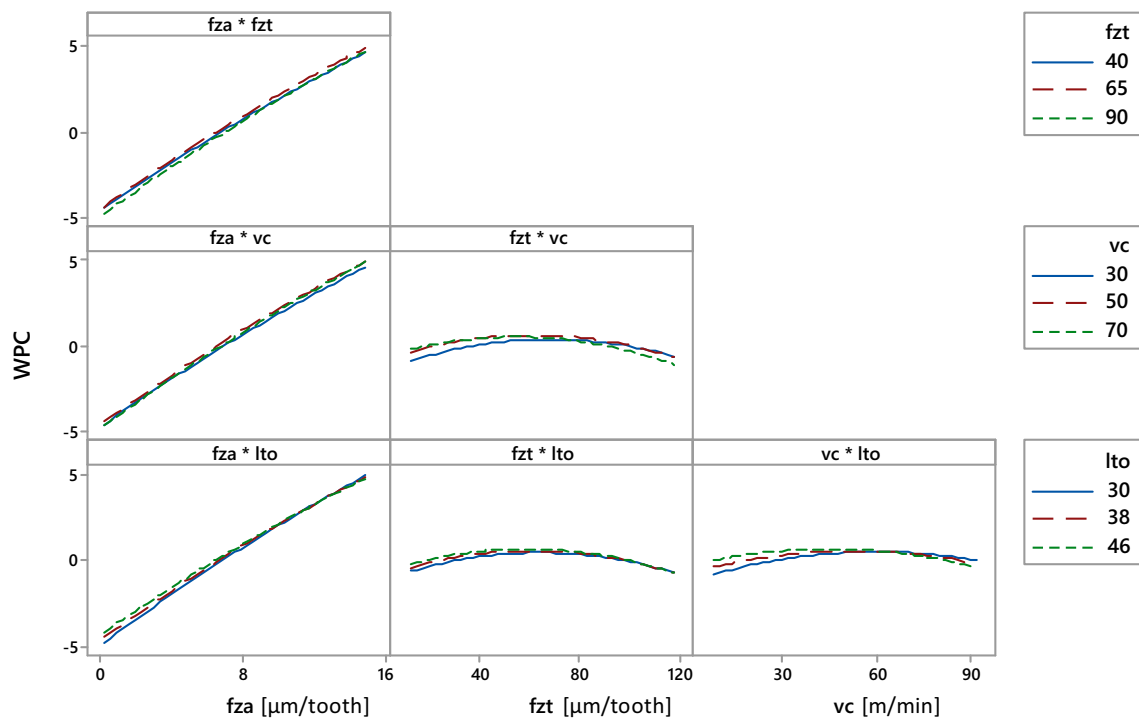| Statistics	F_a	F_r	WPC
$\hat{\sigma}^2$	1.11	1.40	1.30
R^2 (%)	98.33	99.98	97.65
R^2_{adj} (%)	96.52	99.95	95.11
R^2_{pred} (%)	83.79	98.57	81.73
LOF (p value)	0.42	0.53	0.17

Fig. 8 Interaction plot for WPC(**x**,**z**) response surface model

length variation. The coefficients of the mean and variance equations of WPC(**x**,**z**), F_a(**x**,**z**) and F_r(**x**,**z**) are in Eqs. (33–38).

Multivariate robust optimal setting for the machining force components in the helical milling process must be obtained by minimizing the mean and variance fitted equations of WPC(**x**,**z**). The achieved optimal levels of the controllable

variables must optimize the original correlated responses F_a and F_r, minimizing the influence of the tool overhang length variation and considering the influence of the variance–covariance structure in the modeling and optimization problem. Figure 9 shows the response surface plots for the mean and variance of WPC(**x**,**z**) under different perspectives.

$$E_z[\text{WPC}(\mathbf{x},\mathbf{z})] = 0.605 + 2.231 f_{za} - 0.074 f_{zt} + 0.051 v_c - 0.087 f_{za}^2 - 0.255 f_{zt}^2 - 0.193 v_c^2 + 0.053 f_{za} \times f_{zt} \\ + 0.046 f_{za} \times v_c - 0.139 f_{zt} \times v_c \tag{33}$$

$$V_z[\text{WPC}(\mathbf{x},\mathbf{z})] = 1.307 - 0.019 f_{za} - 0.011 f_{zt} - 0.029 v_c + 0.009 f_{za}^2 + 0.003 f_{zt}^2 + 0.022 v_c^2 + 0.010 f_{za} \times f_{zt} \\ + 0.028 f_{za} \times v_c + 0.016 f_{zt} \times v_c \tag{34}$$

$$E_z[F_a(\mathbf{x},\mathbf{z})] = 242.575 + 43.100 f_{za} + 7.049 f_{zt} + 2.905 v_c - 9.472 f_{za}^2 - 7.663 f_{zt}^2 - 7.882 v_c^2 - 6.001 f_{za} \times f_{zt} \\ + 2.000 f_{za} \times v_c + 0.393 f_{zt} \times v_c \tag{35}$$

$$V_z[F_a(\mathbf{x},\mathbf{z})] = 27.642 - 47.511 f_{za} - 35.850 f_{zt} - 20.050 v_c + 21.271 f_{za}^2 + 12.110 f_{zt}^2 + 3.788 v_c^2 + 32.100 f_{za} \times f_{zt} \\ + 17.953 f_{za} \times v_c + 13.546 f_{zt} \times v_c \tag{36}$$

$$E_z[F_r(\mathbf{x},\mathbf{z})] = 194.422 + 72.028 f_{za} - 12.407 f_{zt} - 1.429 v_c - 2.059 f_{za}^2 - 2.134 f_{zt}^2 + 1.205 v_c^2 + 7.009 f_{za} \times f_{zt} \\ + 0.973 f_{za} \times v_c - 3.479 f_{zt} \times v_c \tag{37}$$

$$V_z[F_r(\mathbf{x},\mathbf{z})] = 4.594 + 5.327 f_{za} - 11.521 f_{zt} - 0.249 v_c + 2.221 f_{za}^2 + 10.388 f_{zt}^2 + 0.005 v_c^2 - 9.606 f_{za} \times f_{zt} \\ - 0.208 f_{za} \times v_c + 0.449 f_{zt} \times v_c \tag{38}$$

Fig. 9 Surface plots for **a** WPC mean model and **b** WPC variance model
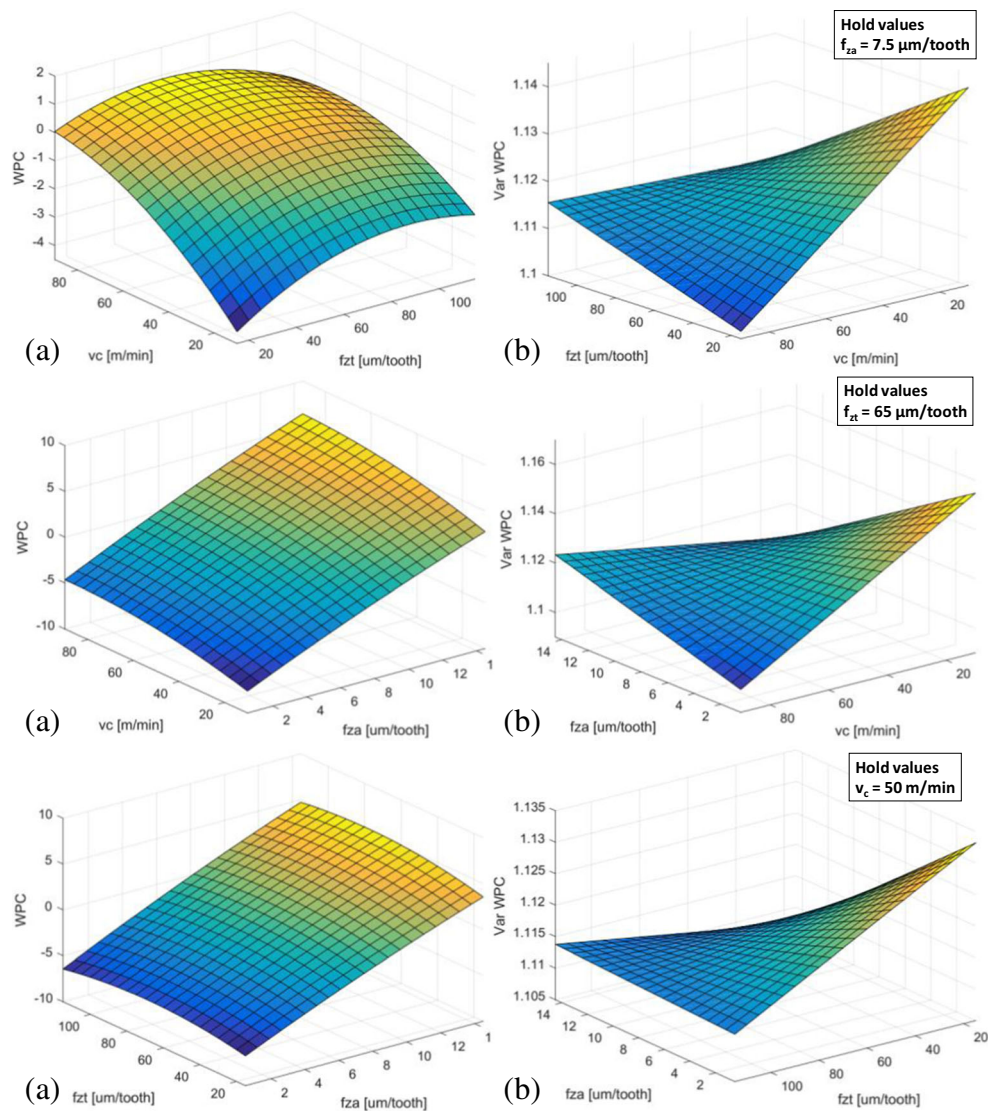
8.4 Utopia, nadir, and payoff matrix calculation for multi-objective optimization

For any multi-objective optimization procedure, it is necessary to calculate the utopia and pseudo nadir for each response, besides the payoff matrix. The utopia points

$$E_z^* \left[\mathbf{x}_{E_z(\text{WPC})}^* \right] = E_z^*(-1.67 \; ; \; 0.16 \; ; \; 0.04) = -3.406$$

and

$$V_z^* \left[\mathbf{x}_{V_z(\text{WPC})}^* \right] = V_z^*(0.28 \; ; \; 0.16 \; ; \; 0.44) = 1.297$$

were obtained as solutions of the non-linear optimization problems $\text{Min}_{\mathbf{x}^T\mathbf{x} \; \le \; 2.828}\{E_z[\text{WPC}(\mathbf{x}, \mathbf{z})]\}$ and $\text{Min}_{\mathbf{x}^T\mathbf{x} \; \le \; 2.828}$

$\{V_z[\text{WPC}(\mathbf{x}, \mathbf{z})]\}$, respectively. Note that WPC can assume negative values because it is standardized and dimensionless. The uncoded levels of the utopia points are E_z^* (1.6 μm/*tooth* ; 69.1 μm/*tooth* ; 50.7 m/min) and V_z^* (8.5 μm/*tooth* ; 69.0 μm/*tooth* ; 58.8 m/min).

The optimal vector for $E_z[\text{WPC}(\mathbf{x}, \mathbf{z})]$ combines the lowest level of $f_{za} = 1.6$ μm/tooth with $f_{zt} = 69.1$ μm/tooth slightly larger than the center point (65.0 μm/tooth), and $v_c = 50.7$ m/min is practically on center point (50.0 m/min). The optimal levels, which minimize the variance of WPC due to the tool overhang length effect, present levels of the controllable factors higher than their center points, with $f_{za} = 8.5$ μm/tooth (center point equals to 7.5 μm/tooth) and $f_{zt} = 69.0$ μm/tooth close of the center point level (65.0 μm/tooth), and $v_c = 58.8$ m/min, which is between its center point (50.0 m/min) and its upper factorial level (70.0 m/min).

The payoff matrix is built using the respective optimal factors levels for $E_z[\text{WPC}(\mathbf{x},\mathbf{z})]$ and $V_z[\text{WPC}(\mathbf{x},\mathbf{z})]$, i.e., −1.67; 0.16; 0.04 and 0.28; 0.16; 0.44. The pseudo nadir points

$$E_z^{\text{PN}}\left[\mathbf{x}_{V_z(\text{WPC})}^*\right] = E_z^{\text{PN}}(0.28 \ ; \ 0.16 \ ; \ 0.44) = 1.187,$$

and

$$V_z^{\text{PN}}\left[\mathbf{x}_{E_z(\text{WPC})}^*\right] = V_z^{\text{PN}}(-1.67 \ ; \ 0.16 \ ; \ 0.04) = 1.356$$

were obtained, which makes it possible to build the payoff matrix Φ as

$$\Phi = \begin{bmatrix} -3.406 & 1.187 \\ 1.356 & 1.297 \end{bmatrix}.$$

8.5 MMSE$_{\text{W}}$-NBI multi-objective optimization

Applying the MMSE$_{\text{W}}$-NBI method iteratively, the optimization results were achieved and are resumed in Table 5.

The Pareto frontier considering $E_z[\text{WPC}(\mathbf{x}, \mathbf{z})] = E_z(\mathbf{x})$ and $V_z[\text{WPC}(\mathbf{x}, \mathbf{z})] = V_z(\mathbf{x})$ is exposed in Fig. 10a. For comparison purposes, the MMSE$_{\text{w}}$, Eq. (24), was solved iteratively and the Pareto frontier is exposed in Fig. 10b. The MMSE$_{\text{w}}$ did not generate an equispaced frontier. On the other hand, the proposed MMSE$_{\text{W}}$-NBI method was efficient in generating equispaced Pareto optimal solutions. It is important to use a Pareto filter to exclude the dominated points from the optimization results. In this study, the MMSE$_{\text{W}}$-NBI method generated four dominated solutions.

The derived results for the mean and variance of F_a and F_r are also resumed in Table 5. It is relevant to state that related to F_a, there were higher levels of Pareto optimal results in terms of mean and variance when compared to the mean and variance levels of F_r. The Pareto optimal results of variance for F_r presented low dispersion. In Table 5, standard deviation (SD) results were also stored since in manufacturing situations this estimate is more useful than the variance estimate.

In Table 5, it is observed that for higher levels of the axial feed per tooth, the expected values for the machining forces are also higher. On the other hand, for lower levels of the

Table 5 MMSE$_{\text{W}}$-NBI optimization results

| | Process variables | | | | | | Responses | | | | | | | |
| | Coded | | | Uncoded | | | $E_z[F_a]$ | $\text{Var}_z[F_a]$ | $\text{SD}_z[F_a]$ | $E_z[F_r]$ | $\text{Var}_z[F_r]$ | $\text{SD}_z[F_r]$ | $E_z[\text{WPC}]$ | $\text{Var}_z[\text{WPC}]$ |
w	f_{za}	f_{zt}	v_c	f_{za} [μm/tooth]	f_{zt} [μm/tooth]	v_c [m/min]	[N]	[N²]	[N]	[N]	[N²]	[N]		
0	0.28	0.16	0.44	8.5	69.0	58.8	254.6	7.1	2.7	212.2	4.2	2.0	1.187	1.297
0.05*	0.09	0.21	0.54	7.8	70.3	60.9	246.7	9.8	3.1	197.3	2.8	1.7	0.728	1.297
0.1*	−0.10	0.26	0.64	7.2	71.6	62.9	238.2	12.9	3.6	182.5	2.0	1.4	0.269	1.297
0.15	−0.28	0.32	0.74	6.5	73.0	64.8	229.3	16.2	4.0	167.9	1.5	1.2	−0.191	1.297
0.2*	−0.46	0.36	0.84	5.9	74.1	66.7	219.8	20.2	4.5	153.5	1.4	1.2	−0.650	1.297
0.25*	−0.63	0.40	0.93	5.3	75.0	68.6	209.8	24.6	5.0	139.3	1.6	1.3	−1.109	1.297
0.3	−0.80	0.41	1.03	4.7	75.4	70.7	199.0	29.9	5.5	125.5	2.1	1.4	−1.569	1.297
0.35	−0.96	0.47	1.11	4.2	76.9	72.3	188.6	34.1	5.8	111.2	2.9	1.7	−2.028	1.297
0.4	−1.10	0.68	1.08	3.7	82.0	71.5	181.4	34.3	5.9	94.3	5.9	2.4	−2.483	1.297
0.45	−1.26	0.62	0.93	3.1	80.6	68.6	173.4	49.7	7.0	83.2	6.1	2.5	−2.774	1.299
0.5	−1.36	0.57	0.81	2.7	79.3	66.2	167.9	62.6	7.9	76.6	6.0	2.4	−2.950	1.303
0.55	−1.43	0.52	0.71	2.5	78.1	64.2	163.8	74.0	8.6	72.1	5.7	2.4	−3.073	1.307
0.6	−1.49	0.48	0.62	2.3	77.0	62.4	160.4	84.6	9.2	68.9	5.5	2.3	−3.164	1.312
0.65	−1.53	0.44	0.54	2.1	75.9	60.7	157.6	94.4	9.7	66.6	5.2	2.3	−3.234	1.317
0.7	−1.57	0.40	0.46	2.0	74.9	59.1	155.2	103.6	10.2	65.0	4.9	2.2	−3.287	1.322
0.75	−1.60	0.36	0.38	1.9	73.9	57.6	153.2	112.3	10.6	63.9	4.5	2.1	−3.328	1.328
0.8	−1.62	0.32	0.31	1.8	72.9	56.1	151.4	120.7	11.0	63.2	4.2	2.0	−3.359	1.333
0.85	−1.64	0.28	0.24	1.8	72.0	54.7	149.9	128.6	11.3	62.9	3.9	2.0	−3.381	1.339
0.9	−1.66	0.24	0.17	1.7	71.0	53.4	148.6	136.4	11.7	63.0	3.5	1.9	−3.396	1.344
0.95	−1.67	0.20	0.10	1.7	70.1	52.0	147.5	143.6	12.0	63.3	3.2	1.8	−3.404	1.350
1	−1.67	0.16	0.04	1.6	69.1	50.7	146.5	150.6	12.3	64.0	2.9	1.7	−3.406	1.356
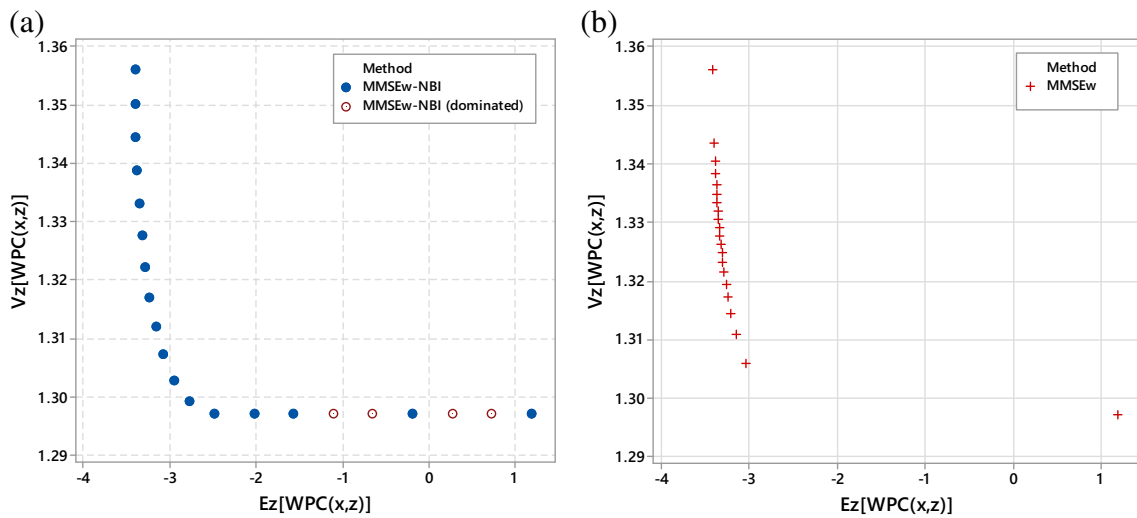
Fig. 10 Pareto frontiers of **a** MMSE$_W$–NBI method and **b** MMSE$_w$ method

axial feed per tooth, the expected values for the machining forces are lower as well. It can be explained by considering the technological characteristic of the helical milling represented by its kinematics and by the two points in Table 5, the points inherent to $w = 0$ and $w = 1$, which have similar levels for the tangential feed per tooth. In this way, the points are $\mathbf{x}^*_{w=0} = [8.5~\mu\text{m/tooth}, 69~\mu\text{m/tooth}, 58.8~\text{m/min}]$ and $\mathbf{x}^*_{w=1} = [1.6~\mu\text{m/tooth}, 69.1~\mu\text{m/tooth}, 50.7~\text{m/min}]$. These points were chosen because they present a great discrepancy between the levels of f_{za} and because this factor is the most significant one for both machining forces. In this line of reasoning, the first point, $\mathbf{x}^*_{w=0}$, has higher levels of the machining forces if compared to the levels of the forces related to the second point, $\mathbf{x}^*_{w=1}$, because the axial cutting depth related to $\mathbf{x}^*_{w=0} = [8.5, 69, 58.8]$, based on Eq. (5), is higher than the axial cutting depth related to $\mathbf{x}^*_{w=1} = [1.6, 69.1, 50.7]$. It is easy to demonstrate this finding through the analysis of the helical milling kinematics. First, through Eqs. (1–4), some helical milling parameters were evaluated. Without loss of generality, they are presented in Table (6).

Table 6 Helical milling parameters for $\mathbf{x}^*_{w=0}$ and $\mathbf{x}^*_{w=1}$

Parameters	$\mathbf{x}^*_{w=0}$	$\mathbf{x}^*_{w=1}$	Unit
f_{za}	0.0085	0.0016	mm
f_{zt}	0.0690	0.0691	mm
v_c	58.8	50.7	m/min
v_{fha}	34.0	6.4	mm/min
v_{ft}	276.0	276.4	mm/min
v_{fht}	92.0	92.1	mm/min
v_f	98.1	92.4	mm/min

The values in Table 6 are important for the calculation of the angle of the helix, Eq. (6). For $\mathbf{x}^*_{w=0} = [8.5; 69; 58.8]$, the angle of the helix is

$$\alpha\left[\mathbf{x}^*_{w=0}\right] = \arctan\left(\frac{34.0}{92.0}\right) = 0.354~radian$$

and for $\mathbf{x}^*_{w=1} = [1.6; 69.1; 50.7]$, the angle of the helix is

$$\alpha\left[\mathbf{x}^*_{w=1}\right] = \arctan\left(\frac{6.4}{92.1}\right) = 0.069~radian$$

By analyzing the angle of the helix related to these two points, it is already easy to realize that due to the higher level of f_{za} in $\mathbf{x}^*_{w=0}$, higher cutting efforts are demanded since f_{za} contributes to the increase of the axial feed velocity of the helix (v_{fha}), increasing the angle of the helix, see Fig. 1, and because f_{za} has a high impact on the cutting forces. To support this statement, the axial cutting depth was also evaluated for better understating these higher efforts requirement. For $\mathbf{x}^*_{w=0} = [8.5, 69, 58.8]$, the axial cutting depth, based on Eq. (5), is

$$a_p^*\left[\mathbf{x}^*_{w=0}\right] = \tan(0.354)\cdot\pi\cdot5 = 5.8~\text{mm}$$

In contrast, for $\mathbf{x}^*_{w=1} = [1.6, 69.1, 50.7]$, the axial cutting depth is

$$a_p^*\left[\mathbf{x}^*_{w=1}\right] = \tan(0.069)\cdot\pi\cdot5 = 1.1~\text{mm}$$

As it is observed, when f_{za} increases, the axial cutting depth increases; both areas that are cut by peripheral and frontal cutting edges also increase, and it requires high cutting efforts, resulting in higher levels of machining forces.
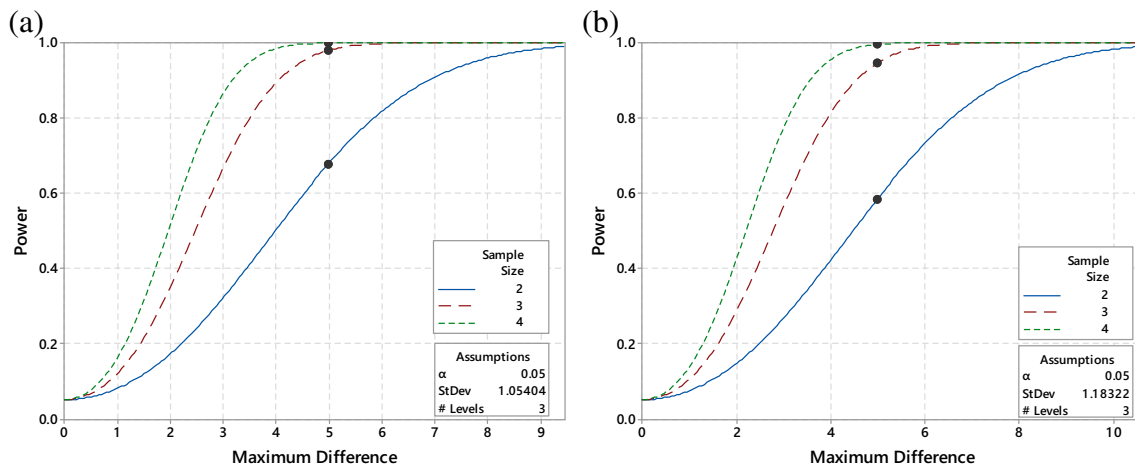
(a)

(b)

Fig. 11 Power curve for **a** F_a and for **b** F_r

8.6 Confirmation runs

Confirmation runs were carried out on the robust Pareto optimal vector $\mathbf{x}^*_{w=0.5} = [-1.36, 0.57, 0.81]$, which in decoded units stands for $\mathbf{x}^*_{w=0.5} = [2.7\ \mu\text{m/tooth}, 79.3\ \mu\text{m/tooth}, 66.2\ \text{m/min}]$. The weight $w = 0.5$ was chosen to guarantee a good compromise between mean and variance. This Pareto optimal vector resulted in $E_z[\text{WPC}] = -2.950$, $Var_z[\text{WPC}] = 1.303$, $E_z[F_a] = 167.9$ N, $SD[F_a] = 7.9$ N, $E_z[F_r] = 76.6$ N, $SD[F_r] = 2.4$ N. The power curve in Fig. 11 guarantees that a sample with $n = 3$ helical milling confirmation tests is sufficient to detect a difference of 5 N in F_a and F_r, considering their respective experimental standard deviations, with probabilities to detect this difference equal to 0.98 and 0.95, respectively.

Table 7 presents the results of the confirmation runs considering the three l_{to} levels and three replications, as determined by the power test. The mean and standard deviation levels obtained for F_a and F_r were $E_z[F_a] = 167.9$ N, with $SD_z[F_a] = 7.9$, $E_z[F_r] = 76.6$ N, with $SD_z[F_r] = 2.4$ N. The Pearson correlation test for F_a and F_r resulted in $r = 0.910$ with p value $= 0.001$. Therefore, the covariance structure between the force components cannot be neglected.

Table 7 Confirmation runs

Run order	l_{to} (mm)	F_a [N]	F_r [N]
1	38	176.8	86.4
2	46	163.6	84.9
3	30	169.9	90.3
4	38	169.0	85.9
5	46	174.9	94.1
6	46	176.2	93.9
7	38	175.9	89.1
8	30	174.4	92.2
9	30	173.8	92.9

To assure homoscedasticity, i.e., the robustness of the Pareto optimal vector $\mathbf{x}^*_{w=0.5} = [-1.36, 0.57, 0.81]$ regarding the l_{to} variation, the Levene's test was performed for F_a and F_r considering the noise factor l_{to} and is resumed in Fig. 12. As the null hypothesis of the Levene's test attests the variance equality and the p values are higher than the significance level, p value $> \alpha = 0.05$, the homoscedasticity of the responses with consideration to the noise factor l_{to} cannot be rejected. In practical terms, it means that the variance regarding the tool overhang length variation is homogeneous in this robust Pareto optimal solution. However, the homogeneity of means regarding this noise factor should also be attested. Then, the MANOVA analysis was performed, considering the three tool overhang length levels (30, 38, 46) and F_a and F_r as responses, to assure more power on conclusions, taking into consideration not only the variances but also the covariance between the responses. Table 8 presents the MANOVA analysis of the confirmation runs considering the correlated responses F_a and F_r against the noise factor l_{to}. It can be stated that the noise factor effect is not significant on the correlated responses since the p values for the three criteria are higher than the significance level, i.e., p value $> \alpha = 0.05$. This means that, considering the optimal vector $\mathbf{x}^*_{w=0.5} = [-1.36, 0.57, 0.81]$, the process is robust to the tool overhang length variation.

Figure 13 shows the confidence intervals for the confirmation runs for F_a and F_r, considering the three different noise factor levels and the robust optimization results. In red reference lines, the predicted robust optimal mean levels are depicted, $F_a^* = 167.9$ N and $F_r^* = 76.6$ N. For F_a, the predicted value was inside of the three confidence intervals with consideration to tool overhang length levels. For F_r, the predicted mean value was inside of only the confidence interval for $l_{to} = 38$ mm. However, the Pareto optimal value for F_r^* also presents a confidence interval associated with its standard deviation $SD_z[F_r] = 2.4$ N.

If intervals do not overlap, the corresponding stdevs are significantly different.
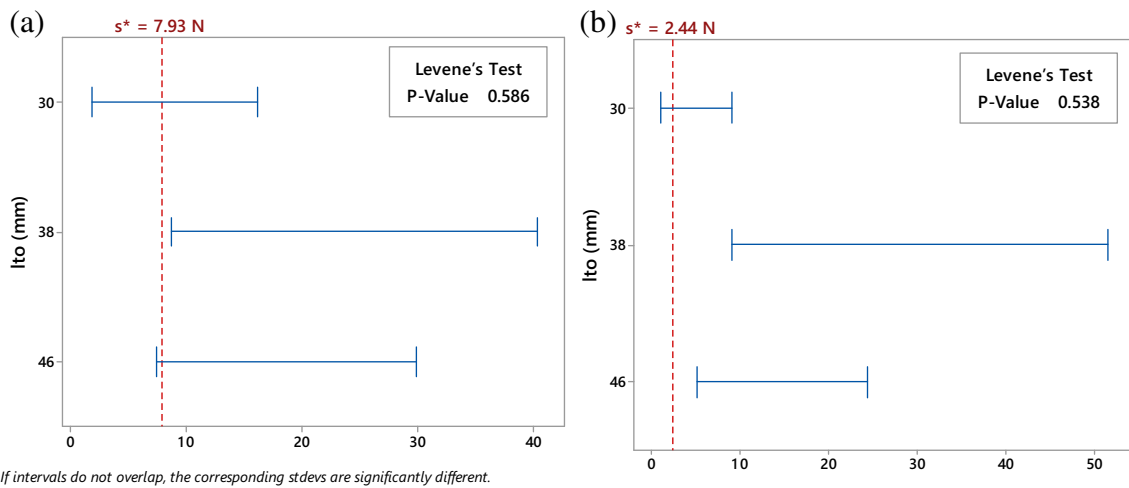
Fig. 12 Levene's test for equal variances. Multiple comparison intervals for the standard deviation, $\alpha = 0.05$. **a** F_a vs l_{to} and **b** F_r vs l_{to}

The confirmation runs showed that the helical milling process of the aluminum alloy Al 7075, considering the correlated responses F_a and F_r, is robust to the tool overhang length variation considering the optimal vector $\mathbf{x}^*_{w=0.5}$. The other Pareto optimal points obtained through the MMSE$_W$–NBI method are also robust to the considered noise factor. Obviously, as the trade-off between mean and variance of the multivariate response, WPC was explored by an equispaced Pareto frontier obtained through the MMSE$_W$–NBI method; the equispaced Pareto points allow to the decision maker the possibility of choosing the desired balance between mean and variance of the correlated responses, which is very important for manufacturing engineers and for multivariate optimization researchers.

8.7 Cutting force models in the workpiece coordinate system and time domain

It is also important to set-up cutting force models in the workpiece coordinate system. In the present approach, the mean and variance models in the tool coordinate system are presented to assure robustness regarding the tool the overhang length variation. The models in the workpiece coordinate system are derived from the models in the tool coordinate system. Therefore, robustness is also achieved in the workpiece coordinate system.

As $F_z = F_a$, the models for mean and variance for F_z are strictly equal to the Eq. (35) and Eq. (36), as presented in Eq. (39) and Eq. (40).

$$E_z(F_z) = 242.575 + 43.100f_{za} + 7.049f_{zt} + 2.905v_c - 9.472f_{za}^2 - 7.663f_{zt}^2 - 7.882v_c^2 - 6.001f_{za} \times f_{zt} + 2.000f_{za} \times v_c + 0.393f_{zt} \times v_c \tag{39}$$

$$V_z(F_z) = 27.642 - 47.511f_{za} - 35.850f_{zt} - 20.050v_c + 21.271f_{za}^2 + 12.110f_{zt}^2 + 3.788v_c^2 + 32.100f_{za} \times f_{zt} + 17.953f_{za} \times v_c + 13.546f_{zt} \times v_c \tag{40}$$

Table 8 MANOVA for F_a and F_r vs l_{to}

Criterion	Test statistic	F	DF		p
			Num	Denom	
Wilks'	0.27	2.30	4	10	0.131
Lawley–Hotelling	2.66	2.66	4	8	0.112
Pillai's	0.74	1.74	4	12	0.205
Roy's	2.65	–	–	–	–
$s = 2$, $m = -0.5$, $n = 1.5$	–	–	–	–	–

The models for F_x and F_y are derived regarding F_r, Eq. (41). Since $F_r = \sqrt{F_x^2 + F_y^2}$, leaving the gap between F_x and F_y aside.

$$F_x = F_y = \frac{1}{\sqrt{2}} F_r \tag{41}$$

Applying the mean operator, one obtains

$$E_z[F_x] = E_z[F_y] = E_z\left[\frac{1}{\sqrt{2}} F_r\right] = \frac{1}{\sqrt{2}} E_z[F_r] \tag{42}$$
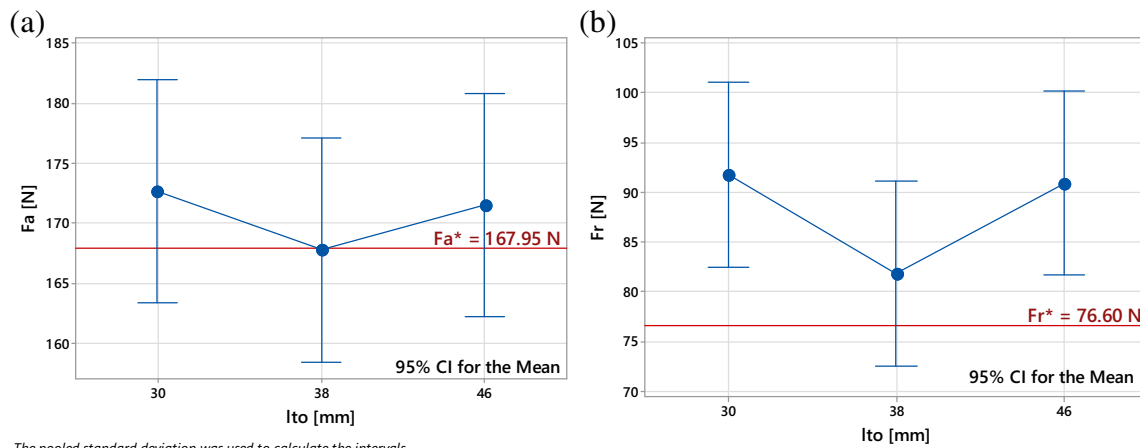
(a)

(b)

Fig. 13 Interval plot of **a** F_a vs l_{to} and **b** F_r vs l_{to}

These models in time domain are defined as follows:

$$E_z[F_x] = \frac{1}{\sqrt{2}} E_z[F_r]\cos(\omega_o \cdot t) \tag{43}$$

$$E_z[F_y] = \frac{1}{\sqrt{2}} E_z[F_r]\sin(\omega_o \cdot t) \tag{44}$$

where ω_o, in radian/second, is the angular velocity of the orbital feed motion, and t, in seconds, is the time. The angular velocity of the orbital feed motion ω_o is calculated according

to Eq. (45), where the orbital rotation speed n_o is obtained according to Eq. (46) [13].

$$\omega_o = \frac{2\pi n_o}{60} \tag{45}$$

$$n_o = \frac{v_{fht}}{\pi \cdot D_h} \tag{46}$$

Finally, replacing Eq. (37) into Eq. (43) and Eq. (44), the models for mean of F_x and F_y are explicitly exposed in Eq. (47) and Eq. (48).

$$E_z(F_x) = \frac{1}{\sqrt{2}} \left\{ \begin{array}{l} 194.422 + 72.028f_{za} - 12.407f_{zt} - 1.429v_c - 2.059f_{za}^2 - 2.134f_{zt}^2 + 1.205v_c^2 + 7.009f_{za} \times f_{zt} \\ +0.973f_{za} \times v_c - 3.479f_{zt} \times v_c \end{array} \right\} \cos(\omega_o \cdot t) \tag{47}$$

$$E_z(F_y) = \frac{1}{\sqrt{2}} \left\{ \begin{array}{l} 194.422 + 72.028f_{za} - 12.407f_{zt} - 1.429v_c - 2.059f_{za}^2 - 2.134f_{zt}^2 + 1.205v_c^2 + 7.009f_{za} \times f_{zt} \\ +0.973f_{za} \times v_c - 3.479f_{zt} \times v_c \end{array} \right\} \sin(\omega_o \cdot t) \tag{48}$$

Analogously, the variance operator may be applied in Eq. (41). By doing so, it may be obtained:

$$V_z[F_x] = V_z[F_y] = V_z\left[\frac{1}{\sqrt{2}}F_r\right] = \frac{1}{2}V_z[F_r] \tag{49}$$

The variance for F_x and F_y may not be obtained in the time domain since variance cannot assume negative values. Explicitly, Eq. (50) provides the variance for F_x and F_y. This equation provides an estimate of the error in the cutting force components on xy plane regarding the tool overhang length variation.

$$V_z(F_x) = V_z(F_y) = \frac{1}{2} \left\{ \begin{array}{l} 4.594 + 5.327f_{za} - 11.521f_{zt} - 0.249v_c + 2.221f_{za}^2 + 10.388f_{zt}^2 + 0.005v_c^2 - 9.606f_{za} \times f_{zt} \\ -0.208f_{za} \times v_c + 0.449f_{zt} \times v_c \end{array} \right\} \tag{50}$$

Fig. 14 Comparison of experimental and modeled cutting force in the workpiece coordinate system. $f_{za} = 2.75$ μm/tooth, $f_{zt} = 79.3$ μm/tooth, and $v_c = 66.2$ m/min
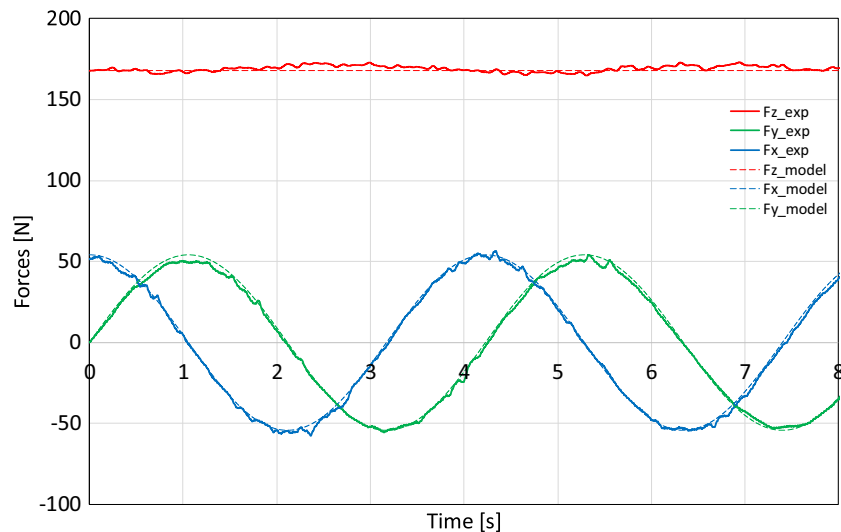
Considering the optimal vector $\mathbf{x}^*_{w=0.5}$, Fig. 14 shows the predicted cutting force in the workpiece coordinate system according to Eq. (39), Eq. (47), and Eq. (48) together with the experimental levels of one of the confirmation runs. As it may be observed, the predicted values were close to the experimental values. However, the propagation of error proposed in RPD with combined array represents in the equation a part of variability regarding the experimental error, which may take into account another noise factor not considered in the present study. Then, the proposed method may be applied in the helical milling considering others noise factors of this process to allow predicting the variability of cutting forces more precisely. It is usual to provide the percentage error of cutting force models regarding experimentally obtained values. However, in the present approach, there is a model to predict the error, i.e., the variance model for each cutting force component. As these models are in function of helical milling parameters, the error of the proposed approach will vary according to the selected Pareto optimal vector in the experimental region. It means that there are experimental levels, which were achieved with the proposed approach MMSE$_W$-NBI, obtained to achieve low variance levels. For the example exposed in Fig. 14, the percentage errors in F_x, F_y, and F_z were 1.05, 0.15, and 0.67%, respectively. In other experimental regions, where the process is not robust regarding the tool overhang length variation, these levels of error may not be guaranteed. Then, it is important to consider the variance models to achieve lower error levels of the mean models regarding experimental levels. Besides, these models work inside the experimental region, i.e., respecting the constraint $\mathbf{x}^T\mathbf{x} = f_{za}{}^2 + f_{zt}{}^2 + v_c{}^2 \leq \rho^2 = 2.828$, in coded units.

9 Conclusions and future works

The present work presented a new multivariate robust modeling and optimization method. The method guarantees the multivariate modeling and optimization of bias and variance of the axial and radial cutting force components of the helical milling process of the aluminum alloy Al 7075. Also, there is no loss of information, through the optimization of the mean and variance equations of the weighted principal component.

The tool overhang length was set as a noise factor since in cavity machining there are specific workpiece geometries that constrain this factor. To complete the set of independent variables, the axial and tangential feed per tooth and cutting velocity were chosen as controllable factors.

The MMSE$_W$-NBI's combination was proposed to allow the replication of the method. The weighted principal component technique was carried out to avoid loss of information and to deal with the correlation problem between the axial and radial cutting force components.

The results showed good determination coefficients for the response surface models of the weighted principal component and the axial and radial cutting force components. The NBI method optimized the mean and variance equations of the weighted principal component. Optimal vectors were replaced in the mean and variance equations of the helical milling outcomes considered in this paper, leading to their robust optimal solutions. Pareto frontiers were plotted considering mean and standard deviation estimates of the weighted principal component, confirming that the MMSE$_W$-NBI method is efficient in generating equiespaced Pareto solutions.

Confirmation runs were carried out on the optimal robust vector $\mathbf{x}^*_{w=0.5} = [2.7$ μm/tooth, 79.3 μm/tooth, 66.2 m/min] with three tool overhang length levels (30, 38, 46) [mm] and three replications. Levene's test revealed that the homoscedasticity of the outcomes with consideration to the noise factor cannot be rejected, i.e., the robustness of the Pareto optimal vector $\mathbf{x}^*_{w=0.5}$ was confirmed. To assure more power on conclusions, the multivariate analysis of variance (MANOVA) was performed considering the confirmation runs; the results showed that the noise factor

effect is not significant on the correlated outcomes, considering the optimal vector.

Besides obtaining mean and variance cutting force models in the tool coordinate system, mean and variance models for the cutting force components were also obtained in the workpiece coordinate system in the time domain. Considering the optimal vector $\mathbf{x}^*_{w=0.5}$, the percentage errors in F_x, F_y, and F_z were only 1.05, 0.15, and 0.67%, respectively. The variance models of the cutting forces regarding the tool overhang length is an important achievement since the experimenter may apply the Pareto optimal experimental solutions to achieve lower error levels for mean models obtained for cutting force components.

For future works, other helical milling responses could be taken into consideration when performing the proposed multivariate robust and optimization method like roughness and geometrical error responses. Furthermore, extra helical milling noise factors could be explored like tool wear, workpiece hardness, workpiece grain sizes, and others. Different multivariate methods could be explored for multivariate statistical analysis. Finally, additional optimization methods could be tested in comparison with NBI and MSE, methods like normalized normal constraint (NNC), ε-constraint, and others that allow the inclusion of multivariate techniques in their routines.

References

1. Iyer R, Koshy P, Ng E (2007) Helical milling: an enabling technology for hard machining precision holes in AISI D2 tool steel. Int J Mach Tools Manuf 47(2):205–210. https://doi.org/10.1016/j.ijmachtools.2006.04.006

2. Pilný L, De Chiffre L, Píška M, Villumsen MF (2012) Hole quality and burr reduction in drilling aluminum sheets. CIRP J Manuf Sci Technol 5(2):102–107. https://doi.org/10.1016/j.cirpj.2012.03.005

3. Sheth S, George PM (2016) Experimental investigation, prediction and optimization of cylindricity and perpendicularity during drilling of WCB material using grey relational analysis. Precis Eng 45:33–43. https://doi.org/10.1016/j.precisioneng.2016.01.002

4. Brinksmeier E, Fangmann S, Rentsch R (2011) Drilling of composites and resulting surface integrity. CIRP Ann - Manuf Technol 60(1):57–60. https://doi.org/10.1016/j.cirp.2011.03.077

5. Li H, He G, Qin X, Wang G (2014) Tool wear and hole quality investigation in dry helical milling of Ti-6Al-4V alloy. Int J Adv Manuf Technol 71(5-8):1511–1523. https://doi.org/10.1007/s00170-013-5570-0

6. Li Z, Liu Q (2012) Surface topography and roughness in holemaking by helical milling. Int J Adv Manuf Technol 66:1415–1425

7. Qin X, Gui L, Li H, Rong B, Wang D, Zhang H et al (2012) Feasibility study on the minimum quantity lubrication in high-speed helical milling of Ti-6Al-4V. J Adv Mech Des Syst Manuf 6(7):1222–1233. https://doi.org/10.1299/jamdsm.6.1222

8. Brinksmeier E, Fangmann S, Meyer I (2008) Orbital drilling kinematics. Prod Eng Res Devel 2(3):277–283. https://doi.org/10.1007/s11740-008-0111-7

9. Sasahara H, Kawasaki M, Tsutsumi M (2008) Helical feed milling with MQL for boring of aluminum alloy. J Adv Mech Des Syst Manuf 2(6):1030–1040. https://doi.org/10.1299/jamdsm.2.1030

10. Fang Q, Pan Z, Fei S, Xie X, Ke Y (2015) A novel helical milling end-effector and its application. IEEE/ASME Trans Mechatron 20(6):3112–3122. https://doi.org/10.1109/TMECH.2015.2409986

11. Tanaka H, Ohta K, Takizawa R, Yanagi K (2012) Experimental study on tilted planetary motion drilling for CFRP. Procedia CIRP 1:443–448. https://doi.org/10.1016/j.procir.2012.04.079

12. Denkena B, Boehnke D, Dege JH (2008) Helical milling of CFRP–titanium layer compounds. CIRP J Manuf Sci Technol 1(2):64–69. https://doi.org/10.1016/j.cirpj.2008.09.009

13. Pereira RBD, Brandão LC, Paiva AP, Ferreira JR, Davim JP (2017) A review of helical milling process. Int J Mach Tools Manuf 120:27–48. https://doi.org/10.1016/j.ijmachtools.2017.05.002

14. Ventura CEH, Hassui A (2013) Modeling of cutting forces in helical milling by analysis of tool contact angle and respective depths of cut. Int J Adv Manuf Technol 68(9-12):2311–2319. https://doi.org/10.1007/s00170-013-4837-9

15. Wang H, Qin X, Ren C, Wang Q (2011) Prediction of cutting forces in helical milling process. Int J Adv Manuf Technol 58:849–859

16. Corne R, Nath C, El Mansori M, Kurfess T (2017) Study of spindle power data with neural network for predicting real-time tool wear/breakage during inconel drilling. J Manuf Syst 43:287–295. https://doi.org/10.1016/j.jmsy.2017.01.004

17. Haiyan W, Xuda Q (2016) A mechanistic model for cutting force in helical milling of carbon fiber-reinforced polymers. Int J Adv Manuf Technol 82(9-12):1485–1494. https://doi.org/10.1007/s00170-015-7460-0

18. Tian Y, Liu Y, Wang F, Jing X, Zhang D, Liu X (2017) Modeling and analyses of helical milling process. Int J Adv Manuf Technol 90(1-4):1003–1022. https://doi.org/10.1007/s00170-016-9418-2

19. Wang H, Qin X, Li H, Tan Y (2016) A comparative study on helical milling of CFRP/Ti stacks and its individual layers. Int J Adv Manuf Technol 5:1973–1983

20. Shan Y, He N, Li L, Zhao W, Qin X (2011) Orbital milling hole of aerospace Al-alloy with big pitch. Trans of Tianjin Univ 17(5):329–335. https://doi.org/10.1007/s12209-011-1637-x

21. Liu C, Wang G, Dargusch MS (2012) Modelling, simulation and experimental investigation of cutting forces during helical milling operations. Int J Adv Manuf Technol 63(9-12):839–850. https://doi.org/10.1007/s00170-012-3951-4

22. Rey PA, LeDref J, Senatore J, Landon Y (2016) Modelling of cutting forces in orbital drilling of titanium alloy Ti-6Al-4V. Int J Mach Tools Manuf 106:75–88. https://doi.org/10.1016/j.ijmachtools.2016.04.006

23. Li ZL, Ding Y, Zhu LM (2017) Accurate cutting force prediction of helical milling operations considering the cutter runout effect. Int J Adv Manuf Technol 92(9–12):4133–4144

24. Mishra V, Khan GS, Chattopadhyay KD, Nand K, Sarepaka RV (2014) Effects of tool overhang on selection of machining parameters and surface finish during diamond turning. Measurement 55:353–361. https://doi.org/10.1016/j.measurement.2014.05.019

25. Kiyak M, Kaner B, Sahin I, Aldemir B, Cakir O (2010) The dependence of tool overhang on surface quality and tool wear in the turning process. Int J Adv Manuf Technol 51(5-8):431–438. https://doi.org/10.1007/s00170-010-2654-y

26. Rama Kotaiah K, Srinivas J, Sekar M (2009) Prediction of optimal stability states in inward-turning operation using neurogenetic algorithms. Int J Adv Manuf Technol 45(7-8):679–689. https://doi.org/10.1007/s00170-009-2007-x

27. Kull Neto H, Diniz AE, Pederiva R (2016) Influence of tooth passing frequency, feed direction, and tool overhang on the surface

roughness of curved surfaces of hardened steel. Int J Adv Manuf Technol 82(1-4):753–764. https://doi.org/10.1007/s00170-015-7419-1

28. Basu S, Dan PK, Thakur A (2014) Experimental design in soap manufacturing for optimization of fuzzified process capability index. J Manuf Syst 33(3):323–334. https://doi.org/10.1016/j.jmsy.2014.03.001

29. Myers RH, Khuri AI, Vining G (1992) Response surface alternatives to the Taguchi robust parameter design approach. Am Stat 46:131–139

30. Nair VN, Abraham B, Mackay J, Box G, Kacker RN, Lorenzen TJ et al (1992) Taguchi's parameter design: a panel discussion. Technometrics 34(2):127–161. https://doi.org/10.1080/00401706.1992.10484904

31. Welch W, Yu T, Kang SM, Sacks J (1990) Computer experiments for quality control by parameter design. J Qual Technol 22:15–22

32. Shoemaker AC, Tsui KL, CFJ W (1991) Economical experimentation methods for robust design. Technometrics 33(4):415–427. https://doi.org/10.1080/00401706.1991.10484870

33. Box G, Jones S (1992) Designing products that are robust to the environment. Total Qual Manag 3(3):265–282. https://doi.org/10.1080/09544129200000034

34. Box G (1998) Signal-to-noise ratios, performance criteria, and transformations. Technometrics 30:1–17

35. Lin DKJ, Tu W (1995) Dual response surface optimization. J Qual Technol 27:34–39

36. Köksoy O (2006) Multiresponse robust design: mean square error (MSE) criterion. Appl Math Comput 175:1716–1729

37. Paiva AP, Paiva EJ, Ferreira JR, Balestrassi PP, Costa SC (2009) A multivariate mean square error optimization of AISI 52100 hardened steel turning. Int J Adv Manuf Technol 43(7-8):631–643. https://doi.org/10.1007/s00170-008-1745-5

38. Paiva AP, Campos PH, Ferreira JR, Lopes LGD, Paiva EJ, Balestrassi PP (2012) A multivariate robust parameter design approach for optimization of AISI 52100 hardened steel turning with wiper mixed ceramic tool. Int J Refract Met Hard Mater 30(1):152–163. https://doi.org/10.1016/j.ijrmhm.2011.08.001

39. Paiva AP, Gomes JHF, Peruchi RS, Leme RC, Balestrassi PP (2014) A multivariate robust parameter optimization approach based on principal component analysis with combined arrays. Comput Ind Eng 74:186–198. https://doi.org/10.1016/j.cie.2014.05.018

40. Box GEP, Hunter WG, Macgregor JF, Erjavec J (1973) Some problems associated with the analysis of multiresponse data. Technometrics 15(1):33–51. https://doi.org/10.1080/00401706.1973.10489009

41. Johnson RA, Wichern DW (2007) Applied multivariate statistical analysis, 6th edn. Pearson Prentice-Hall, New Jersey

42. Liao HC (2006) Multi-response optimization using weighted principal component. Int J Adv Manuf Technol 27(7-8):720–725. https://doi.org/10.1007/s00170-004-2248-7

43. Rencher AC (2002) Methods of multivariate analysis, 2nd edn. John Wiley & Sons, New York. https://doi.org/10.1002/0471271357

44. FC W, Chyu CC (2004) Optimization of correlated multiple quality characteristics robust design using principal component analysis. J Manuf Syst 23:134–143

45. Das I, Dennis JE (1998) Normal-boundary intersection: a new method for generating the Pareto surface in nonlinear multicriteria optimization problems. SIAM J Optim 8(3):631–657. https://doi.org/10.1137/S1052623496307510

46. Ganesan T, Vasant P, Elamvazuthi I (2013) Normal-boundary intersection based parametric multi-objective optimization of green sand mould system. J Manuf Syst 32(1):197–205. https://doi.org/10.1016/j.jmsy.2012.10.004

47. Zhang Q, Liou JJ, McMacken J, Thomson J, Layman P (2001) Development of robust interconnect model based on design of experiments and multiobjective optimization. IEEE Trans Electron Devices 48(9):1885–1891. https://doi.org/10.1109/16.944173

48. Brito TG, Paiva AP, Ferreira JR, Gomes JHF, Balestrassi PP (2014) A normal boundary intersection approach to multiresponse robust optimization of the surface roughness in end milling process with combined arrays. Precis Eng 38(3):628–638. https://doi.org/10.1016/j.precisioneng.2014.02.013

49. Costa DMD, Paula TI, Silva PAP, Paiva AP (2016) Normal boundary intersection method based on principal components and Taguchi's signal-to-noise ratio applied to the multiobjective optimization of 12L14 free machining steel turning process. Int J Adv Manuf Technol 87(1-4):825–834. https://doi.org/10.1007/s00170-016-8478-7

50. Das I, Dennis JE (1996) Normal boundary intersection: an alternate method for generating Pareto optimal points in multicriteria optimization problems. NASA Contractor Report 201616, ICASE Report No. 96–62

51. Paiva AP, Costa SC, Paiva EJ, Balestrassi PP, Ferreira JR (2010) Multi-objective optimization of pulsed gas metal arc welding process based on weighted principal component scores. Int J Adv Manuf Technol 50(1-4):113–125. https://doi.org/10.1007/s00170-009-2504-y

52. Jia Z, Ierapetritou MG (2007) Generate Pareto optimal solutions of scheduling problems using normal boundary intersection technique. Comput Chem Eng 31(4):268–280. https://doi.org/10.1016/j.compchemeng.2006.07.001

53. Lopes LGD, Brito TG, Paiva AP, Peruchi RS, Balestrassi PP (2016) Robust parameter optimization based on multivariate normal boundary intersection. Comput Ind Eng 93:55–66. https://doi.org/10.1016/j.cie.2015.12.023

54. Haggag AA (1981) A variant of the generalized reduced gradient algorithm for non-linear programming and its applications. Eur J Oper Res 7:161–168

55. Pereira RBD, Leite RR, Alvim AC, Paiva AP, Ferreira JR, Davim JP (2017) Multi-objective robust optimization of the sustainable helical milling process of the aluminum alloy Al 7075 using the augmented- enhanced normalized normal constraint method. J Clean Prod 152:474–496. https://doi.org/10.1016/j.jclepro.2017.03.121

56. Li Z, Liu Q, Ming X, Wang X, Dong Y (2014) Cutting force prediction and analytical solution of regenerative chatter stability for helical milling operation. Int J Adv Manuf Technol 73(1-4):433–442. https://doi.org/10.1007/s00170-014-5793-8